OXFORD

Human Molecular Genetics, 2026, 1–17
https://doi.org/10.1093/hmg/ddaf199
Original Article

TULP1 missense mutations cause variable retinal phenotypes and activation of the endoplasmic reticulum unfolded protein response pathway

Ke Jiang[1,2], Satyabrata Sinha[1], Vera L. Bonilha[1,2], Minzhong Yu[1,2], Neal S. Peachey[1,2,3], Stephanie A. Hagstrom[1,2,*]

[1]Department of Ophthalmic Research, Cole Eye Institute, Cleveland Clinic, Cleveland, OH 44195, United States
[2]Department of Ophthalmology, Cleveland Clinic Lerner College of Medicine of Case Western Reserve University, Cleveland, OH 44195, United States
[3]Louis Stokes Cleveland VA Medical Center, Cleveland, OH 44106, United States

*Corresponding author: 9500 Euclid Ave, Cleveland, OH 44195. E-mail: hagstrs@ccf.org

Abstract

Mutations in *TULP1* are associated with early-onset forms of inherited retinal degenerations (IRDs). Evidence from *Tulp1*$^{-/-}$ mice indicates that TULP1 plays a role in photoreceptor protein trafficking. Here we generated two novel knock-in mouse models, each expressing the ortholog to a human IRD-causing homozygous missense *TULP1* mutation to: 1) better recapitulate IRD patients' gene dosage and spatiotemporal degeneration, 2) determine the pathological disease mechanism, and 3) evaluate mutations affecting different domains of the protein. The *Tulp1*^{F492L} model carries a mutation affecting a conserved amino acid in the C-terminal tubby domain, whereas the *Tulp1*^{D89Y} model carries the only homozygous mutation located outside the tubby domain. In both mutant retinas, TULP1^{F492L} and TULP1^{D89Y} protein levels and distribution were comparable to WT. Surprisingly, variable retinal phenotypes were observed in the two mutant lines. The *Tulp1*^{F492L} model displayed rapid photoreceptor degeneration, rod and cone opsin mistrafficking, and abnormal shaped ribbon synapses, similar to *Tulp1*$^{-/-}$ mice. In contrast, these abnormalities were not seen in the *Tulp1*^{D89Y} model; indeed, retinal morphology and function was preserved up to 12 months, although we noted less RPE pigmentation and dilated structures in the outer plexiform layer at this timepoint. Moreover, building on our prior *in vitro* results, we observed activation of the IRE1 branch of the endoplasmic reticulum (ER)-unfolded protein response (UPR) complex in *Tulp1*$^{-/-}$ and *Tulp1*^{F492L} retinas, identifying ER stress as a key disease mechanism leading to photoreceptor death and as a potential therapeutic target in *TULP1*-associated forms of IRD.

Keywords: inherited retinal disease; photoreceptor degeneration; TULP proteins; ERUPR

Introduction

Inherited retinal degenerations (IRDs) constitute a spectrum of clinically and genetically heterogeneous group of diseases targeting the photoreceptor and/or retinal pigment epithelial (RPE) cells of the retina. The prevalence of IRDs affects approximately 1 in 4000 individuals worldwide and can result in profound vision loss, impacting abilities that depend on high acuity vision and overall quality of life [1, 2]. The clinical diversity ranges from non-progressive, pan-retinal disorders such as night blindness and cone dysfunction to progressive conditions such as retinitis pigmentosa (RP) and Leber congenital amaurosis (LCA) to focal macular degenerations [3]. To date, more than 400 genes have been identified to cause IRDs and more than 3000 mutations have been reported in these genes (RetiGene, https://retigene.erdc.info/; access date 12/2025). Remarkably, different mutations within the same gene can be associated with drastically different phenotypes leading to different IRD diagnoses. Conversely, phenotypically similar IRDs may arise from mutations in different genes, generating layers of complexity to the diagnosis and understanding of the pathophysiology of IRDs.

One example highlighting this wide range of clinical heterogeneity in IRDs is the gene *TULP1*. We first identified biallelic mutations in *TULP1* in patients with autosomal recessive RP (ARRP) [4]. Since then, *TULP1* mutations have been found associated with various forms of IRDs, including RP, early-onset RP, LCA, cone-rod dystrophy (CRD), and cone dystrophy [5–10]. To date, ~100 disease-causing *TULP1* mutations have been identified (www.lovd.nl/gene; access date 12/2025) and the prevalence of *TULP1* mutations is estimated to be between 2–3% of all IRD cases in European and North American cohorts, with 4500 individuals worldwide who are estimated to have biallelic mutations [10–14]. In Arab cohorts, however, it reaches up to 14%, reflecting founder mutations and a high degree of consanguinity [15]. Most patients carrying *TULP1* mutations exhibit rod-driven forms of the disease, whereas a fraction of patients exhibit cone-driven disease.

TULP1 is a member of the Tubby-like family of proteins (TULPs), including TUB and TULPs 1–4, which are characterized by the signature conserved C-terminal 'tubby domain' of ~250 amino acids mediating phosphoinositide (PIP) plasma membrane binding and the divergent N-terminal disordered region facilitating distinct

Received: August 21, 2025. **Revised:** December 15, 2025. **Accepted:** December 22, 2025

functions [16–18]. The majority of *TULP1* IRD-associated mutations are missense variants located in the tubby domain followed by protein-truncating mutations scattered throughout the gene. As with many IRD-causing genes, *TULP1* is expressed in photoreceptor cells of the retina, specifically in the inner segments, connecting cilium, perikarya and synaptic terminal. *Tulp1* knock-out (*Tulp1*$^{-/-}$) mice have been generated and develop an early-onset, progressive photoreceptor degeneration similar to the rapid degeneration described in IRD patients with *TULP1* mutations [19, 20]. In this model, defects occur in both the outer segment (OS) and synaptic compartments of the photoreceptor cell prior to the onset of degeneration. The visual pigments, rhodopsin, cone opsins and several other OS-specific phototransduction proteins, are mislocalized throughout all photoreceptor cellular compartments [19, 21]. In addition, the photoreceptor synapses lack the tight spatial relationship between ribbon-associated proteins, leading to impaired neurotransmitter vesicular release and attenuation of bipolar cell dendrites [22, 23]. Cumulative evidence from studying *Tulp1*$^{-/-}$ mice indicates that the protein likely functions as an adapter for protein trafficking from the photoreceptor inner segment (IS) to the OS and as an organizer of vesicular trafficking in the photoreceptor ribbon synapse to second order neurons [20–23].

Mouse models are useful tools to investigate pathological mechanisms underlying photoreceptor degeneration and to assist in evaluating potential therapeutic strategies for IRDs. However, to our knowledge, only global knock-out models of *Tulp1* exist (*Tulp1*$^{-/-}$ and *Tulp1*^{tvrm124}) [20, 24]. To better recapitulate IRD patients' gene dosage and spatiotemporal retinal degeneration and to add to the spectrum of mutant *Tulp1* mouse lines in which to decipher the pathophysiological mechanism of disease, we generated two novel *Tulp1* knock-in mouse models each expressing a homozygous *TULP1* IRD-associated missense mutation using CRISPR/Cas9 gene editing technology. One mutation affects an amino acid in the tubby domain (F492L), corresponding to the human IRD-causing *TULP1* F491L mutation, and the other affects a residue in the divergent region (D89Y), corresponding to the human IRD-causing *TULP1* D94Y mutation. In this study, comprehensive structural and functional analyses were performed on the *Tulp1*^{D89Y} and *Tulp1*^{F492L} knock-in mice over a range of ages and compared to wild-type (WT) and *Tulp1*$^{-/-}$ mice. Our findings indicate that the *Tulp1*^{F492L} mouse model accurately recapitulates the photoreceptor degeneration seen in patients with the corresponding *TULP1* missense mutation. However, the *Tulp1*^{D89Y} model reveals a strikingly different disease course, indicating variable retinal phenotypes between the different *Tulp1* genetic models and leading to novel information regarding domain-specific mutations. Moreover, we provide evidence of endoplasmic reticulum (ER) stress leading to activation of the unfolded protein response (UPR) in *Tulp1* mutant animal models, establishing that the ER-UPR is a key mechanism by which photoreceptor degeneration occurs in *TULP1*-associated forms of IRD.

Results

Generation of Tulp1 knock-in mice

To study the pathogenic effect of the human IRD-causing *TULP1* homozygous missense mutations D94Y and F491L, we introduced each mutation into the corresponding locus within the mouse genome, via CRISPR/Cas9 gene editing technology. We designated these models *Tulp1*^{D89Y} and *Tulp1*^{F492L}, corresponding to the mouse amino acid. Each mouse line has a stable genomic integration of a mutation affecting the endogenous mouse *Tulp1* gene. For each independent mouse line, the induced DNA break was repaired through microhomology-mediated end joining by a template containing the desired mutations. We generated the *Tulp1*^{F492L} model to evaluate a common human mutation affecting a conserved amino acid (A.A.) in the C-terminal tubby domain, which leads to different forms of IRDs in patients; and the *Tulp1*^{D89Y} model to evaluate the only known homozygous IRD-causing missense mutation affecting the N-terminal domain (Fig. 1A) [4, 25]. Importantly, we examined the evolutionary conservation of A.A. D89 and found that it is highly conserved across mammals (Fig. 1B). A.A. F492 is located in the mutation 'hot spot' tubby domain and is also very highly conserved across TULP1 orthologs (Fig. 1C). Homozygous mice for each knock-in allele were identified through direct sequence analysis (Fig. 1D and E). The general appearance of *Tulp1*^{D89Y} and *Tulp1*^{F492L} mutant mice were indistinguishable from WT littermates and there was no developmental delay, fertility concerns or gross dysmorphic features.

Distribution of mutant TULP1 in the retina

The distribution of mutant TULP1 protein in the knock-in mouse retinas was examined by immunohistochemistry at P17 (Fig. 2A) and P23 (Fig. 2B) and compared to that in WT and *Tulp1*$^{-/-}$ mice. We chose these two ages because at P17, photoreceptor development is complete in WT mice, but precedes photoreceptor cell death in *Tulp1*$^{-/-}$ mice; whereas at P23, photoreceptor degeneration has commenced in *Tulp1*$^{-/-}$ mice [20, 22]. Consistent with previous results, TULP1 is localized to the inner segment (IS), connecting cilium (CC), perikarya of the outer nuclear layer (ONL), and synaptic terminals (OPL) of photoreceptor cells in WT mouse retina at both ages [19, 20]. The localization of mutant TULP1 in both the *Tulp1*^{D89Y} and *Tulp1*^{F492L} (Fig. 2A and B) retinas appears similar to that in the WT retina with a comparable amount of immunoreactivity seen in the IS, CC, and OPL at both timepoints. No immunostaining is detected in the *Tulp1*$^{-/-}$ retina (Fig. 2A and B). To further assess the distribution of mutant TULP1 protein in the IS and CC region in detail, we co-stained P17 *Tulp1*^{D89Y} and *Tulp1*^{F492L} retinal sections with antibodies against TULP1 and a cilia marker acetyl-α Tubulin and compared to WT. In both *Tulp1*^{D89Y} and *Tulp1*^{F492L} retinas, mutant TULP1 proteins are properly localized to IS and CC region with comparable immunoreactivity intensity as in WT retina (Fig. 2C). These results indicate that the photoreceptor distribution of TULP1^{D89Y} and TULP1^{F492L} protein is not grossly affected in the retina.

Characterization of photoreceptor degeneration in Tulp1 knock-in mice

The retinal morphology of *Tulp1* knock-in mice were evaluated by light microscopy at multiple timepoints and compared to WT and *Tulp1*$^{-/-}$ mice (Fig. 3). At P17, all three *Tulp1* mutant retinas (*Tulp1*^{D89Y}, *Tulp1*^{F492L}, and *Tulp1*$^{-/-}$) show normal morphology with complete retinal lamination and a full complement of photoreceptor nuclei (Fig. 3A). Quantification of the ONL thickness shows that no significant cell loss was detected at P17 in all three mutant models (Fig. 3F). Progressive thinning of the ONL was observed from P23 onward in both the *Tulp1*^{F492L} and *Tulp1*$^{-/-}$ retinas, showcasing the time course of photoreceptor degeneration (Fig. 3B-E). By P23 the ONL was significantly reduced in *Tulp1*^{F492L} and *Tulp1*$^{-/-}$ retinas compared to WT (Fig. 3F). We also observed shortened IS and OS at this age in both mutant retinas (Fig. 3B). Thinning of the ONL progressed in *Tulp1*^{F492L} and *Tulp1*$^{-/-}$ retinas at 1 month of age (Fig. 3C). Notably, the degenerative phenotype of the *Tulp1*^{F492L}

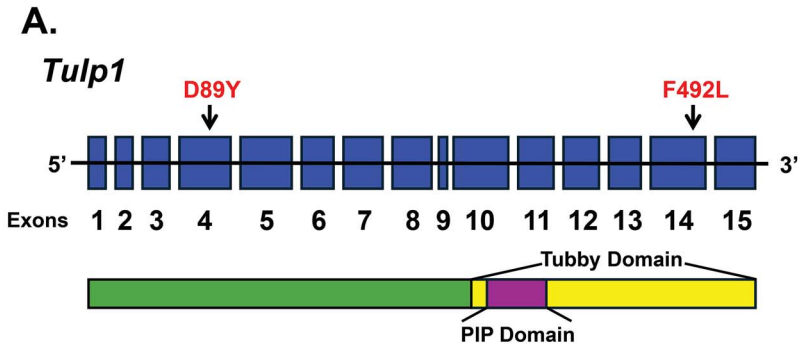

B.

Organism	Accession #	A.A. #	D89	A.A. #
H. Sapiens (human)	NP_003313.3	84	PQTVYARFLRDPEAKKRDPRE	104
P. Troglodytes (chimpanzee)	XP_063669335.1	109	PQTVYARFLRDPEAKKRDPRE	129
M. Mulatta (monkey)	XP_028703469.1	84	PQTVYARFLRDPEAKKRDPRE	104
C. Lupus (dog)	XP_038538769.1	120	PQTVYAKFLRDPEAKRDPRET	140
B. Taurus (cattle)	NP_001193657.1	80	AQTVYTKFLRDPEAKKRDPRE	100
M. Musculus (mouse)	NP_067453.1	79	AQTVYAKFLRDPEAKKRDPRE	99
R. Norvegicus (rat)	NP_001401996.1	80	EQTVYAKFLRDPEAKKRDPRE	100
S. Scrofa (pig)	XP_020954290.1	171	PRTDYTKFLRDPEAKKRDPRD	191
O. Cuniculus (rabbit)	XP_069930256.1	85	QPSVYAKFLRDPEAKKPDPRE	105

C.

Organism	Accession #	A.A. #	F492	A.A. #
H. Sapiens (human)	NP_003313.3	481	GRVTQASVKNFQIVHADDPDY	501
P. Troglodytes (chimpanzee)	XP_063669335.1	506	GRVTQASVKNFQIVHADDPDY	526
M. Mulatta (monkey)	XP_028703469.1	480	GRVTQASVKNFQIVHADDPDY	500
C. Lupus (dog)	XP_038538769.1	525	GRVTQASVKNFQIVHADDPDY	545
B. Taurus (cattle)	NP_001193657.1	485	GRVTQASVKNFQIVHADDPDY	505
M. Musculus (mouse)	NP_067453.1	482	GRVTQASVKNFQIVHADDPDY	502
R. Norvegicus (rat)	NP_001401996.1	483	GRVTQASVKNFQIVHADDPDY	503
S. Scrofa (pig)	XP_020954290.1	574	GRVTQASVKNFQIVHADDPDY	594
O. Cuniculus (rabbit)	XP_069930256.1	485	GRVTQASVKNFQIVHADDPDY	505
G. Gallus (chicken)	XP_046760122.1	517	GRVTHASVKNFQIVHGSDPDY	537
X. Tropicalis (frog)	NP_001016482.1	455	GRVTHPSVKNFQIVHADDLDY	475

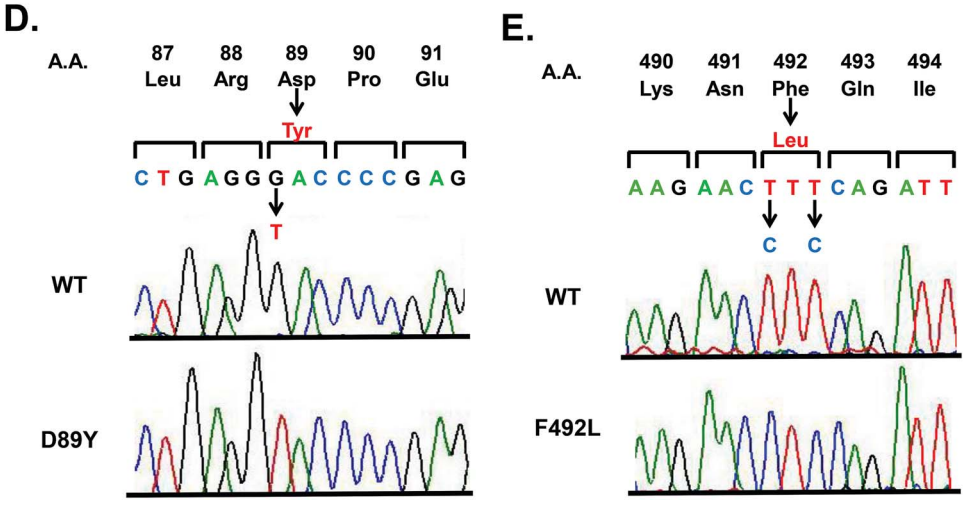

Figure 1. Generation of the *Tulp1* knock-in mice. (A) Schematic diagram of the two target sites at the mouse *Tulp1* locus. The D89Y and F492L mutations are shown in red, the conserved tubby domain is highlighted in yellow, and the PIP-binding motif in purple. (B) Multiple sequence alignments showing the high conservation of a.a. D89 in TULP1, highlighted in yellow, within mammals. (C) Multiple sequence alignments showing the high conservation of a.a. F492 in TULP1, highlighted in red, within vertebrates. (D) Sequence chromatogram of exon 4 in *Tulp1* confirming the presence of the D89Y homozygous mutation in founder mice. (E) Sequence chromatogram of exon 14 in *Tulp1* confirming the presence of the F492L homozygous mutation in founder mice.

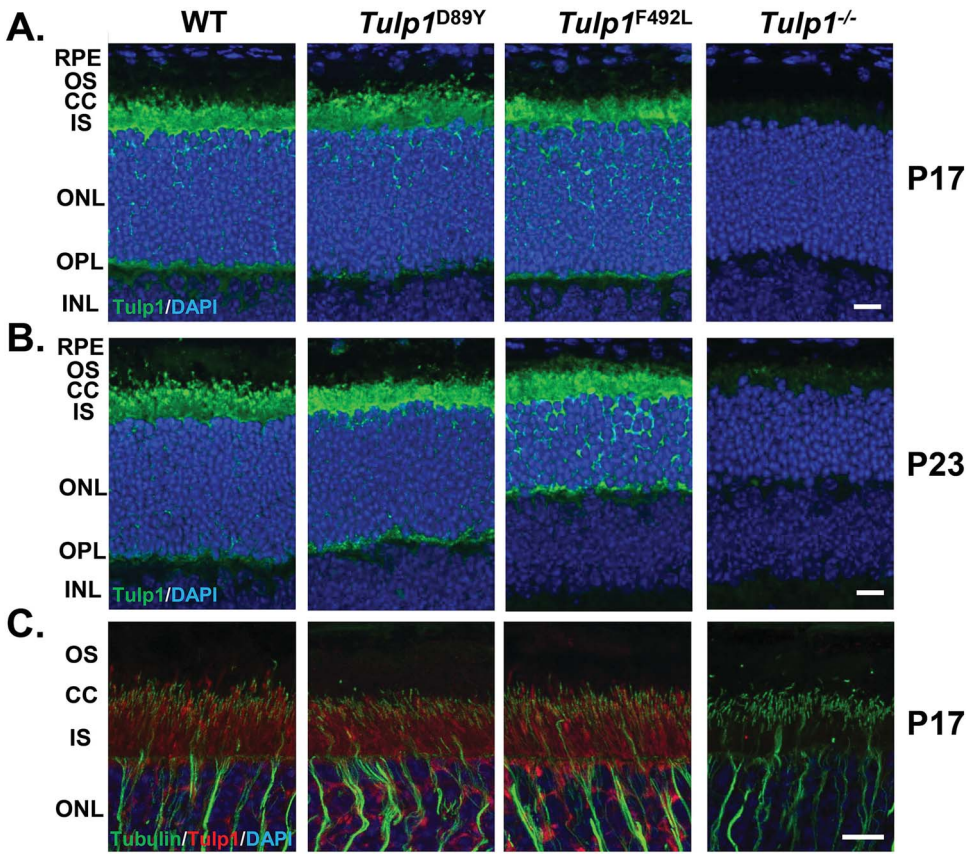

Figure 2. Immunolocalization of TULP1 protein in mouse retinas. At P17 (A) and P23 (B) TULP1 (green) has a similar distribution in WT and *Tulp1* mutant retinas. At both ages, TULP1 is localized to the IS, CC, perikarya of the ONL, and OPL of photoreceptor cells in WT, *Tulp1*^{D89Y} and *Tulp1*^{F492L} retinas; and is not expressed in the *Tulp1*$^{-/-}$ retina. Blue indicates nuclear DAPI stain. Scale bar = 10 um. (C) Co-staining of TULP1 (red) and cilia marker acetyl-α tubulin (green) showed normal distribution of mutant TULP1 protein in *Tulp1*^{D89Y} and *Tulp1*^{F492L} retinas in IS and CC region at P17. Blue indicates nuclear DAPI stain. Scale bar = 10 um. RPE: Retinal pigment epithelium, OS: Outer segment, CC: Connecting cilium, IS: Inner segment, ONL: Outer nuclear layer, OPL: Outer plexiform layer, INL: Inner nuclear layer.

model was less severe than seen in *Tulp1*$^{-/-}$ retinas at both P23 and 1 month of age (Fig. 3F). At 2 months of age, both *Tulp1*^{F492L} and *Tulp1*$^{-/-}$ retinas reach an advanced stage of degeneration, showing a more significant loss of photoreceptor nuclei with only 2–3 rows remaining, and severe IS and OS atrophy (Fig. 3D). Figure 3E reveals an end stage photoreceptor degeneration at 4 months of age in the *Tulp1*^{F492L} and *Tulp1*$^{-/-}$ retinas with only one row of nuclei remaining in the ONL and complete loss of IS and OS. Contrary to the other two mutant models, the morphology of the *Tulp1*^{D89Y} retina is comparable to WT between P17 and 4 months of age with no statistical difference in ONL thickness, suggesting no evidence of photoreceptor cell loss during this time frame. Overall, these results indicate that the degenerative phenotype varies significantly across the different *Tulp1* mutant models.

To test retinal function across the mutant *Tulp1* mouse lines, we performed electroretinography (ERG) at comparable ages. Figure 4 presents a series of dark-adapted ERGs obtained from 4–6 representative mice per genotype at P17 (A), P23 (B), 2 months (C) and 4 months (D). At P17, there is an overall reduction in both the a- and b-wave amplitudes in the *Tulp1*$^{-/-}$ response, consistent with earlier studies showing that this is an early-onset physiological phenotype independent of anatomy (Fig. 4A). At this same timepoint, there was also a mild reduction in the a- and b-wave amplitudes in the *Tulp1*^{F492L} mutant as compared to WT. This reduction progressed with increasing age from P23 to 4 months in both *Tulp1*$^{-/-}$ and *Tulp1*^{F492L} retinas and was consistent with the thinned ONL observed by histology at these same timepoints (Fig. 4B-D). In stark contrast, the ERG a- and b-amplitudes of the *Tulp1*^{D89Y} mutant remained comparable to WT at all timepoints examined. Of all three *Tulp1* mutant models examined, the *Tulp1*$^{-/-}$ showed the greatest reduction in both the a- and b-wave followed by the *Tulp1*^{F492L} mutant.

The light-adapted cone ERG was also measured in all *Tulp1* mutant models. Figure 5 presents a series of cone ERGs obtained from 4–6 representative mice per genotype at P17 (A), P23 (B), 2 months (C) and 4 months (D). By P23, the ERG amplitude of *Tulp1*^{F492L} and *Tulp1*$^{-/-}$ mutants were clearly reduced in comparison to WT and *Tulp1*^{D89Y} (Fig. 5B). Responses of *Tulp1*^{F492L} and *Tulp1*$^{-/-}$ mutants progressively decline with increasing age while those of *Tulp1*^{D89Y} remained comparable to WT (Fig. 5B-D). Similar to the dark-adapted ERG analysis, the cone ERG amplitude of the *Tulp1*^{D89Y} mutant was comparable to WT at all timepoints. Results from both the dark- and light-adapted ERG analyses correlate with our histological analysis and strengthen the conclusion that the photoreceptor degeneration varies significantly with genotype in these different *Tulp1* mutant models.

Photoreceptor protein trafficking defects in Tulp1 knock-in mice

Our previous studies have shown that a subgroup of OS-specific proteins are mistrafficked in *Tulp1*$^{-/-}$ retinas [19–21]. Here we analyzed the localization of several OS-specific proteins in the *Tulp1*

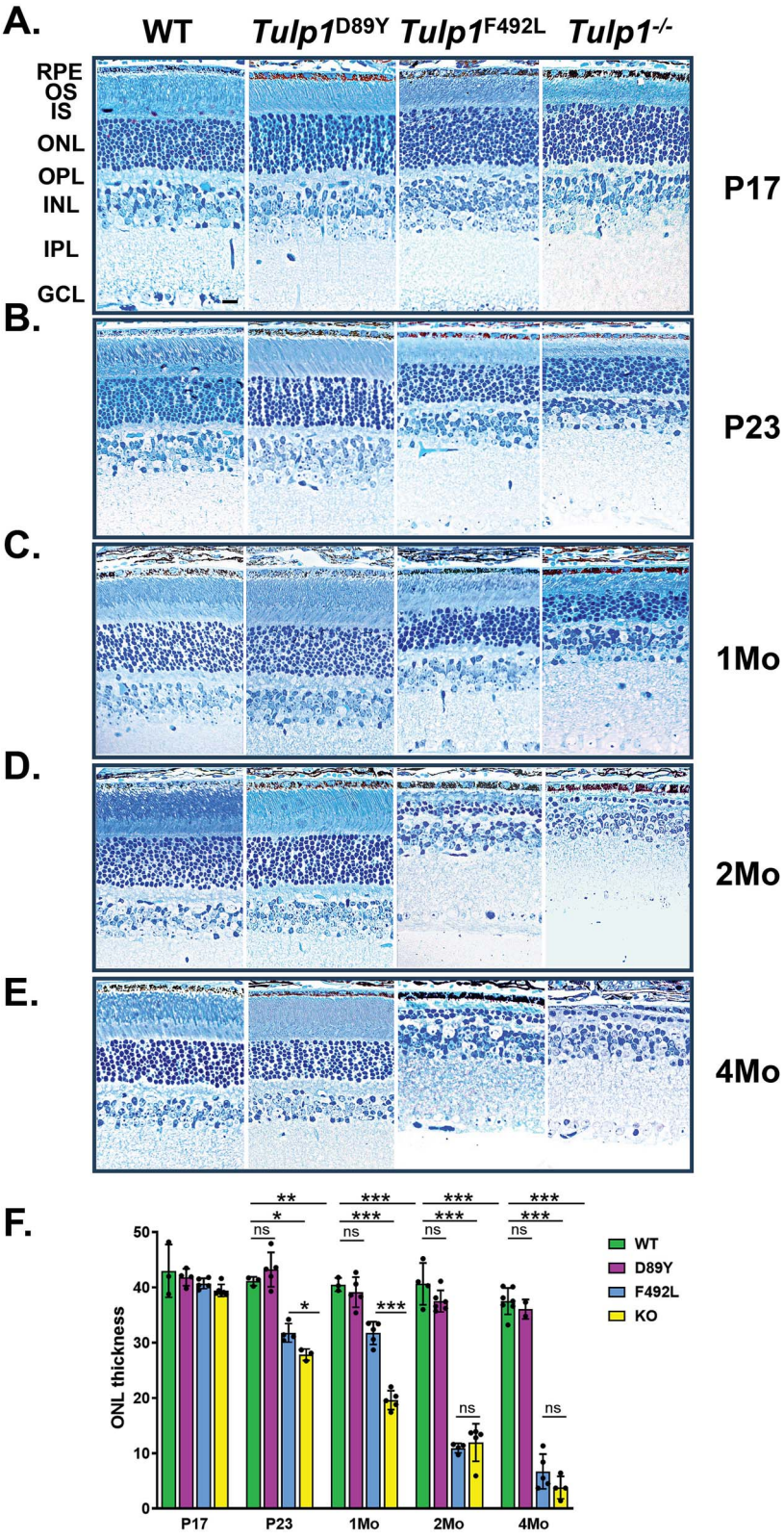

Figure 3. Light microscopy of WT, *Tulp1*^{D89Y}, *Tulp1*^{F492L} and *Tulp1*$^{-/-}$ mouse retinal sections stained with toluidine blue at (A) P17, (B) P23, (C) 1 month, (D) 2 months, and (E) 4 months. Loss of ONL thickness is detected at P23 and progresses rapidly in the *Tulp1*^{F492L} and *Tulp1*$^{-/-}$ retinas. In comparison to the other two mutant models, the morphology of the *Tulp1*^{D89Y} retina is comparable to WT between P17 and 4 months of age. (F) Quantification summary of age-related changes in ONL thickness. Data points indicate the average (±SD) from N = 3–7 mice. Two-tailed Student's t-test, *$P < 0.05$, **$P < 0.01$, ***$P < 0.001$. NS = not significant. Scale bar = 10 um. RPE: Retinal pigment epithelium, OS: Outer segment, IS: Inner segment, ONL: Outer nuclear layer, OPL: Outer plexiform layer, INL: Inner nuclear layer, IPL: Inner plexiform layer, GCL: Ganglion cell layer.

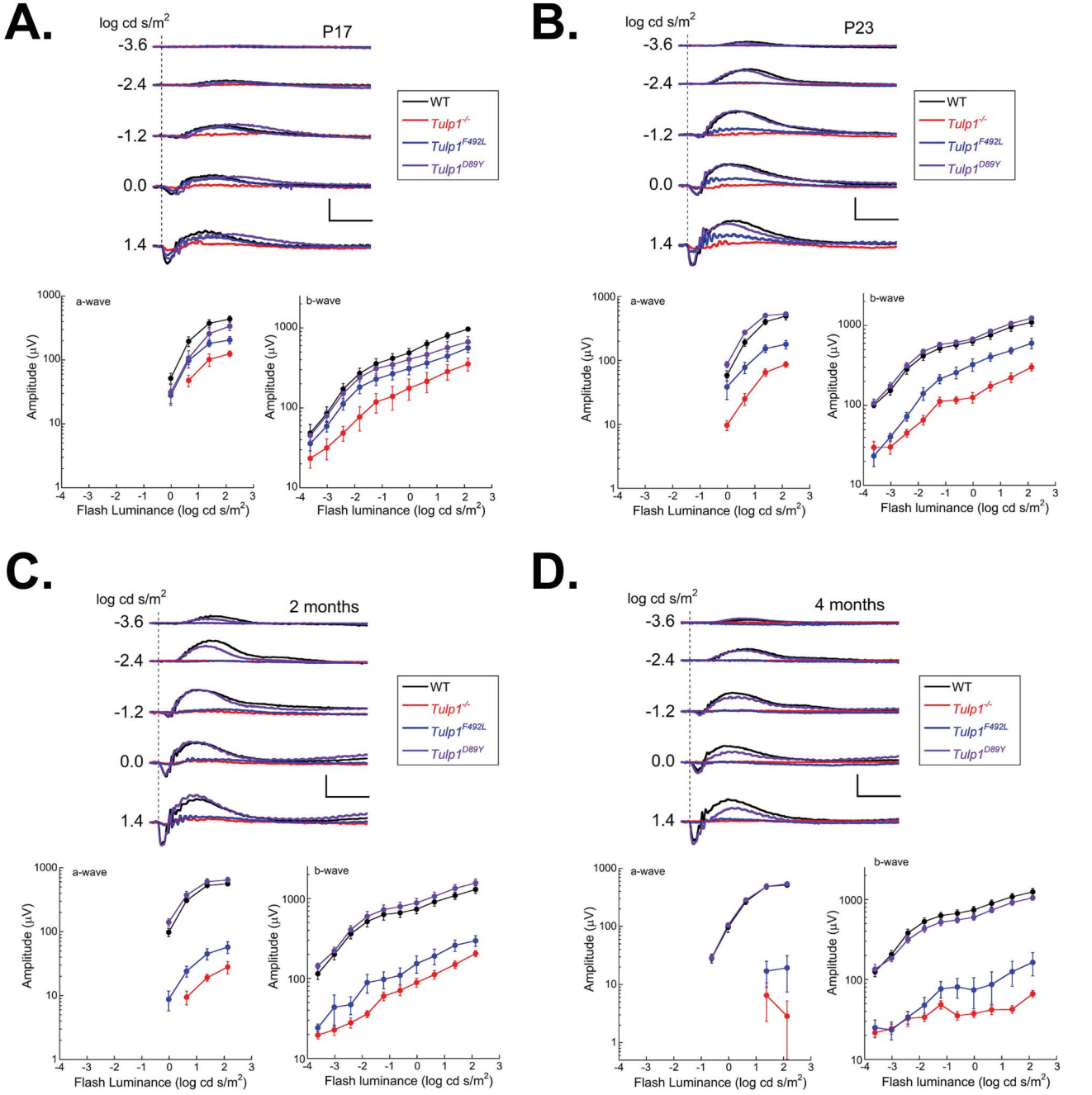

Figure 4. Dark-adapted electroretinography. Summary of dark-adapted ERGs obtained from WT, *Tulp1*^{D89Y}, *Tulp1*^{F492L} and *Tulp1*$^{-/-}$ mice at (A) P17, (B) P23, (C) 2 months, and (D) 4 months of age. In each panel, the upper plot compares representative waveforms while the lower panels present summary luminance-response functions for the a-wave and b-wave components. Scale bars indicate 500 μV and 100 ms. Data points indicate the average (±SEM) for 4–6 mice.

mutant retinas compared to WT at P17 using well-characterized antibodies. Figure 6A reveals that at P17, rhodopsin is correctly transported and retained in the photoreceptor OS in the *Tulp1*^{D89Y} retina, similar to WT. However, in both the *Tulp1*^{F492L} and *Tulp1*$^{-/-}$ retinas, rhodopsin is distributed throughout all photoreceptor compartments. A similar result is seen at P23 (data not shown). To examine cone photoreceptors, we immunostained retinal sections with antibodies against the two cone opsins, short-wavelength cone opsin (S-opsin) and middle-wavelength cone opsin (M-opsin). Figure 6B and C shows that at P17 both the S- and M-cone opsins are correctly trafficked and retained in the OS of the *Tulp1*^{D89Y} mutant mice, comparable to WT. In contrast, both cone opsins are mislocalized throughout all photoreceptor compartments in the *Tulp1*^{F492L} mutant, like that seen in the *Tulp1*$^{-/-}$ (Fig. 6B and C). Mislocalization of the opsins is not likely due to failed OS development as previous results have shown that *Tulp1*$^{-/-}$ retina develop OSs, which can also be appreciated by our histological analysis in Fig. 3A [19–21]. We also analyzed the distribution of another OS-structural protein, peripherin, required for the formation and maintenance of the OS discs. Peripherin is known to traffic to the OS via a different pathway than the opsins [26, 27]. Consistent with our previous results, peripherin localizes correctly to the OS in the *Tulp1*$^{-/-}$ photoreceptors (Fig. 6D). Not surprisingly, peripherin is also correctly trafficked and retained in the photoreceptor OSs in the *Tulp1*^{D89Y} and *Tulp1*^{F492L} mutant retinas (Fig. 6D).

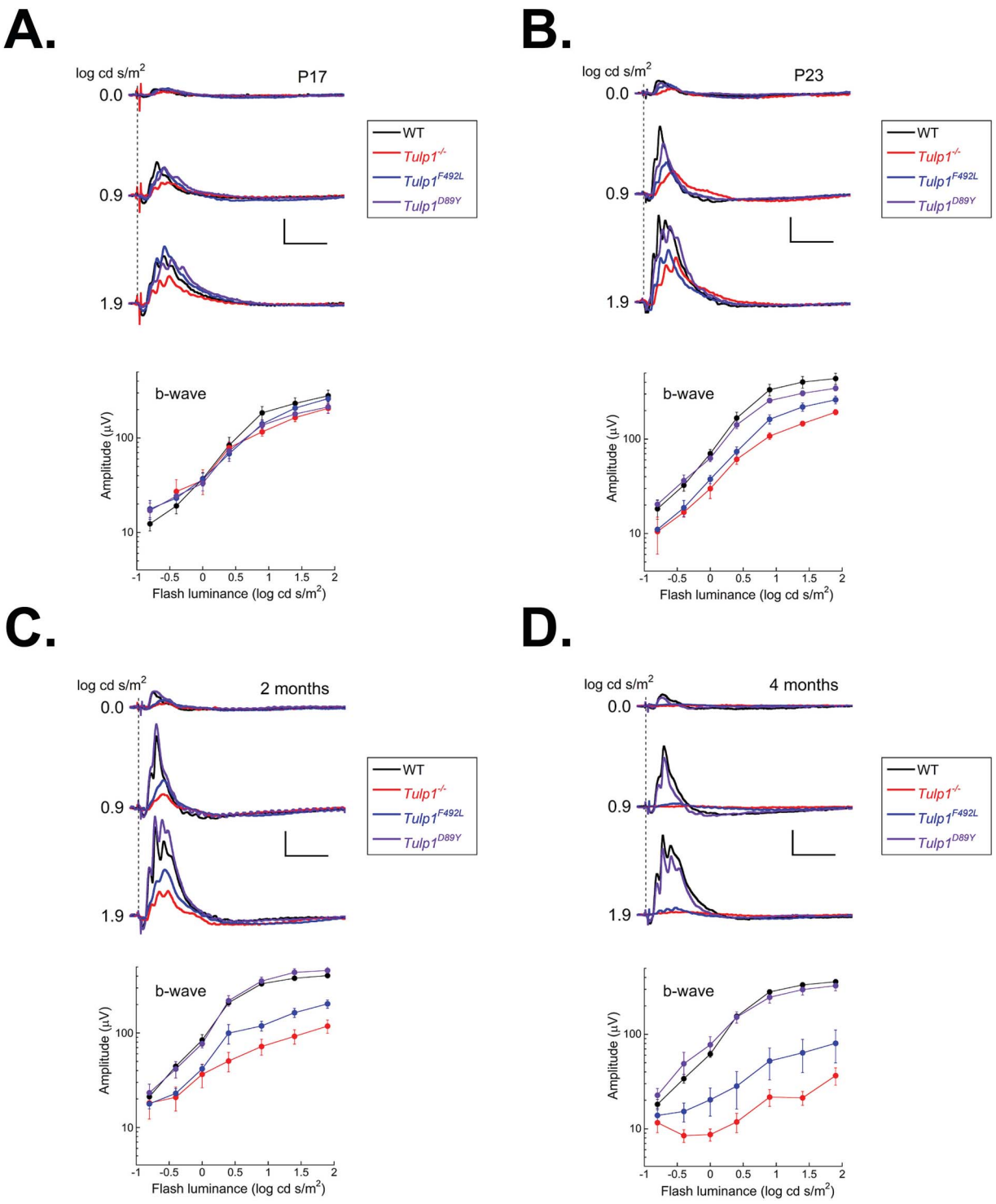

Figure 5. Light-adapted electroretinography. Summary of light-adapted ERGs obtained from WT, *Tulp1*^{D89Y}, *Tulp1*^{F492L} and *Tulp1*$^{-/-}$ mice at (A) P17, (B) P23, (C) 2 months, and (D) 4 months of age. In each panel, the upper plot compares representative waveforms while the lower panels present summary luminance-response functions for the cone b-wave. Scale bars indicate 100 μV and 100 ms. Data points indicate the average (±SEM) for 4–6 mice.

Photoreceptor synaptic defects in Tulp1 knock-in mutant mice

Next, we focused on whether the *Tulp1* knock-in mutants revealed photoreceptor synaptic defects, a phenotypic feature previously identified in the *Tulp1*$^{-/-}$ retina [22]. We examined the synaptic terminal architecture at ages before (P17) and following the start of degeneration (P23) using antibodies against Ribeye/CtBP2, a 120-kDa protein that constitutes the central scaffold of the ribbon. Ribeye normally localizes at the presynaptic membrane in a horseshoe-like shape. Figure 7A and B shows that at both P17 and P23, the OPL of the WT retina contains a multitude of distinct horseshoe-shaped Ribeye-positive ribbons (white arrows). A similar pattern is seen in the *Tulp1*^{D89Y} retina at both ages (Fig. 7A and B). Consistent with previous results, a profoundly

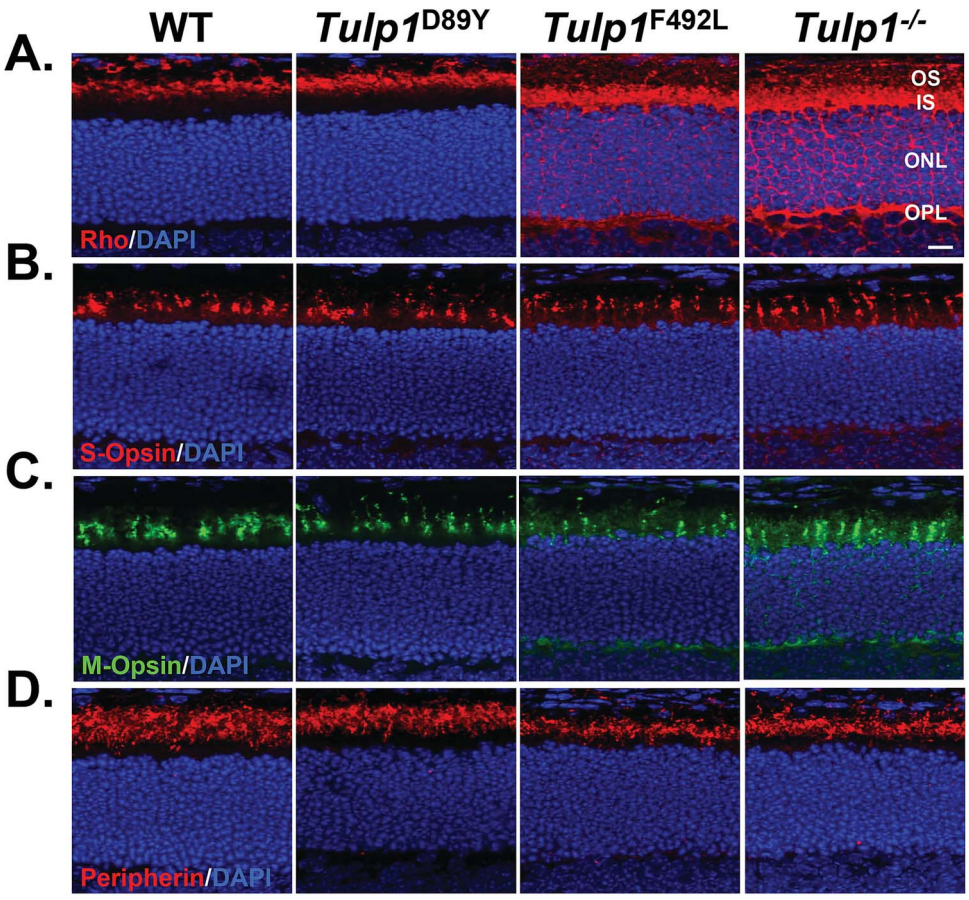

Figure 6. Immunolocalization of OS-specific proteins in WT, *Tulp1*^{D89Y}, *Tulp1*^{F492L} and *Tulp1*$^{-/-}$ mouse retinas at P17. Rhodopsin (A) is restricted to the OS in WT and *Tulp1*^{D89Y} retina but is mislocalized in *Tulp1*^{F492L} and *Tulp1*$^{-/-}$ retinas, with staining appearing in the IS, throughout the ONL, and within the OPL. Localization of short-wavelength cone opsin (S-opsin) (B) is restricted to the OS in WT and *Tulp1*^{D89Y} retina but is also mislocalized in *Tulp1*^{F492L} and *Tulp1*$^{-/-}$ retinas, with staining appearing in the IS, throughout the ONL, and within the OPL. Middle-wavelength cone opsin localization (M-opsin) (C) is restricted to the OS in WT and *tulp1*^{D89Y} retina but is mislocalized in *Tulp1*^{F492L} and *Tulp1*$^{-/-}$ retinas, with staining appearing in the IS, throughout the ONL, and within the OPL. Peripherin (D) is restricted to the OS in WT, *Tulp1*^{D89Y}, *Tulp1*^{F492L} and *Tulp1*$^{-/-}$ mouse retinas. Blue indicates nuclear DAPI stain. Scale bar = 10 um. OS: Outer segment, IS: Inner segment, ONL: Outer nuclear layer, OPL: Outer plexiform layer.

different appearance of Ribeye structure and distribution is seen in the *Tulp1*$^{-/-}$ retina and also in the *Tulp1*^{F492L} retina at both P17 and P23 (Fig. 7A and B). In contrast to the typical horseshoe-shaped ribbons in WT mice, Ribeye staining in the *Tulp1*$^{-/-}$ and *Tulp1*^{F492L} retinas appear punctate and malformed (yellow arrows), and normal-shaped ribbons are rarely seen. These abnormalities are more pronounced at P23 where the OPL of both *Tulp1*^{F492L} and *Tulp1*$^{-/-}$ retinas appear much thinner than WT (Fig. 7B).

Age-related defects in Tulp1^{D89Y} mice

To investigate whether *Tulp1*^{D89Y} mice eventually develop photoreceptor defects, we evaluated mutant retinas at 12 months of age. Histological analysis shows that there are minimal changes in general retinal morphology in the *Tulp1*^{D89Y} retina compared to WT at 12 months (Fig. 8A). However, there appears to be less pigmentation of the RPE and the OPL of the *Tulp1*^{D89Y} retina appears to be thinner in comparison to the WT retina with the presence of dilated structures (black arrowheads) not encountered in WT. Although hard to quantify, these structures were evident when scanning throughout multiple images at this timepoint.

OPL thinning and the presence of dilated structures suggest a reduction in dendritic wiring between photoreceptor and bipolar cells and led us to evaluate the *Tulp1*^{D89Y} mutant mice via ERG. Figure 8B reveals that at 12 months the dark-adapted ERG a- and b-waves amplitudes are somewhat larger than WT in the *Tulp1*^{D89Y} mice, although neither difference reached significance. Under light-adapted conditions, the cone ERG b-waves were significantly reduced in amplitude as compared to WT (Fig. 8C, $P = 0.02$). To define the relationship between the presynaptic and postsynaptic photoreceptor elements, we examined 12 months old *Tulp1*^{D89Y} retinas using antibodies against both Ribeye and Protein Kinase C (PKC), which labels rod depolarizing bipolar cells (DBCs) and their respective dendrites. Figure 9A shows that the PKC-positive DBC dendrites and Ribeye-positive ribbons appear to interact closely in the WT retina (white arrows). In comparison, the DBC dendrites in the *Tulp1*^{D89Y} retina appear shorter and do not extend into the OPL (Fig. 9B). In addition, there are very few normal looking ribbon synapses with the characteristic horseshoe shape as shown by the Ribeye staining (Fig. 9B, yellow arrows). Nevertheless, the *Tulp1*^{D89Y} DBC dendrites and presynaptic ribbons were closely apposed and confined to the OPL, providing at least a minimal platform for photoreceptor-to-bipolar cell transmission, albeit less dense than in WT (Fig. 9B).

ER-UPR activation in Tulp1 mutant mice

Previously, we demonstrated that IRD-associated *TULP1* missense mutations modeled *in silico* and *in-vitro* caused misfolding and

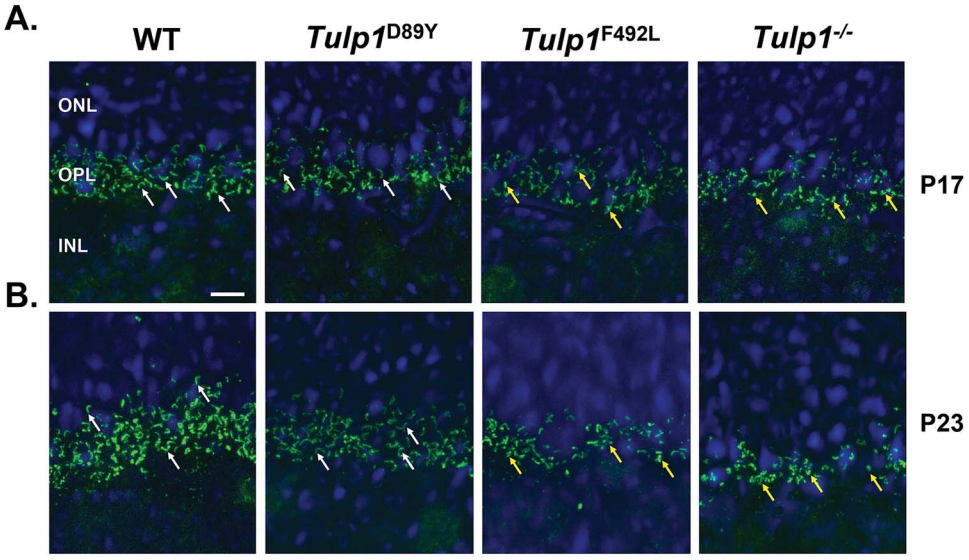

Figure 7. Immunolocalization of Ribeye in the OPL of WT, *Tulp1*^{D89Y}, *Tulp1*^{F492L} and *Tulp1*$^{-/-}$ mouse retinas. At both P17 (A) and P23 (B) Ribeye staining (green) demonstrates that the horseshoe-like appearance of the synaptic ribbons is retained in the WT and *Tulp1*^{D89Y} retinas (white arrows). In contrast, punctate and malformed ribbons (yellow arrows) were observed in *Tulp1*^{F492L} and *Tulp1*$^{-/-}$ retinas at both P17 and P23. At P23, the OPL of *Tulp1*^{F492L} and *Tulp1*$^{-/-}$ retinas appears thinner than that of WT or *Tulp1*^{D89Y} retinas. Scale bar = 5 um. ONL: Outer nuclear layer, OPL: Outer plexiform layer, INL: Inner nuclear layer.

accumulation of the mutant proteins in the endoplasmic reticulum (ER) [28]. We then transiently expressed mutant TULP1 proteins via electroporation in WT mouse retinas at P1, evaluated retinas at P30 (at a time when ~20% of the retina was reliably transfected), and detected activation of the unfolded protein response (UPR) [28]. ER-UPR is a set of pathways activated in response to cellular stress due to accumulation of misfolded and mistrafficked proteins in the ER, in an effort to restore protein homeostasis [29–31]. To determine whether this stress response mechanism is activated in mice expressing a complete knock-in of an IRD-associated *TULP1* mutation, we evaluated key markers corresponding to the IRE1 branch of the ER-UPR, the master regulator in cell fate determination and the most evolutionary conserved branch of ER-UPR pathways (Fig. 10A) [32]. When activated, IRE1 becomes auto-phosphorylated (pIRE1) through its kinase domain, and also activates its C-terminal RNAse domain [32]. The RNase domain of pIRE1 splices an inactive, unspliced form of the transcription factor X-box binding protein 1 (XBP1) (XBP1u, ~29 kDa) to generate an active form, spliced XBP1 (XBP1s, ~48 kDa). XBP1s then enters the nucleus and activates the transcription of chaperone-encoding genes, folding enzymes, and ER-associated protein degradation (ERAD) components to decrease ER stress (Fig. 10A). If not alleviated, prolonged activation can lead to downstream signaling of apoptotic events. We chose to evaluate *Tulp1*^{F492L} retinas at the same timepoint (P30) as that evaluated in our previous transiently expressing overexpression model [28]. Figure 10B shows that retinal lysate from P30 *Tulp1*^{F492L} and *Tulp1*$^{-/-}$ mice express comparable levels of activated IRE1 as in WT mice ($P = 0.63$ and $P = 0.52$, respectively). To determine if the elevated levels of activated IRE1 triggered downstream targets, endogenous levels of XBP1 were evaluated in retinal lysates using an antibody against the N-terminal domain that detects both the spliced and unspliced forms of the protein [33, 34]. Figure 10C reveals that the expression levels of XBP1s in retinal lysate from both *Tulp1*^{F492L} and *Tulp1*$^{-/-}$ mice at P30 are statistically significantly higher than WT retina ($P = 0.04$ and $P = 0.0002$, respectively). Importantly, the observed increasing amount of XBP1s is accompanied by a corresponding decreasing amount of XBP1u in *Tulp1*^{F492L} and *Tulp1*$^{-/-}$ lysate compared to WT, indicating a conversion of the inactive form to the active form of XBP1. P30 represents a mid-stage of photoreceptor degeneration in both *Tulp1*^{F492L} and *Tulp1*$^{-/-}$ mice. At this age, we cannot distinguish whether the activation of ER-UPR plays a key role in the pathogenesis of photoreceptor death or if it is a response to the prolonged cellular stress. Therefore, we further examined whether these proteins are elevated at the onset of photoreceptor degeneration by evaluating retinal lysate from P17 *Tulp1*^{F492L} and *Tulp1*$^{-/-}$ mice. Figure 10D shows that both mutant mice express comparable levels of activated IRE1 as in WT mice ($P = 0.14$ and $P = 0.18$, respectively). However, Fig. 10E reveals that the expression level of XBP1s is statistically significantly higher in only the P17 *Tulp1*$^{-/-}$ lysate with a corresponding decrease in XBP1u ($P = 0.0008$). Although no significant increase in the level of XBP1s was seen in the P17 *Tulp1*^{F492L} lysate compared to WT ($P = 0.34$), an increasing trend is noted albeit with large variability across mice. The *Tulp1*^{D89Y} model was not evaluated because no retinal phenotype was detected at these young ages. Our results provide *in vivo* evidence for the first time that the absence of TULP1 *and* an IRD-causing mutant TULP1 protein activates the IRE1 branch of the ER-UPR stress response pathway.

Discussion

It is well established that mutations in *TULP1* underlie an early-onset, severe form of photoreceptor degeneration, both in humans and mice. Of the >100 IRD-causing *TULP1* mutations, protein-truncating mutations including splice-site, frameshift, nonsense, and missense mutations are distributed throughout the gene, whereas all but five missense mutations are located in the C-terminal conserved tubby domain. Of these five N-terminal missense mutations, only one has been identified homozygously; whereas the other four are compound heterozygotes with the second mutation located in the tubby domain or, in one case, not identified [10, 25, 35–37]. Presently, only two knock-out mouse

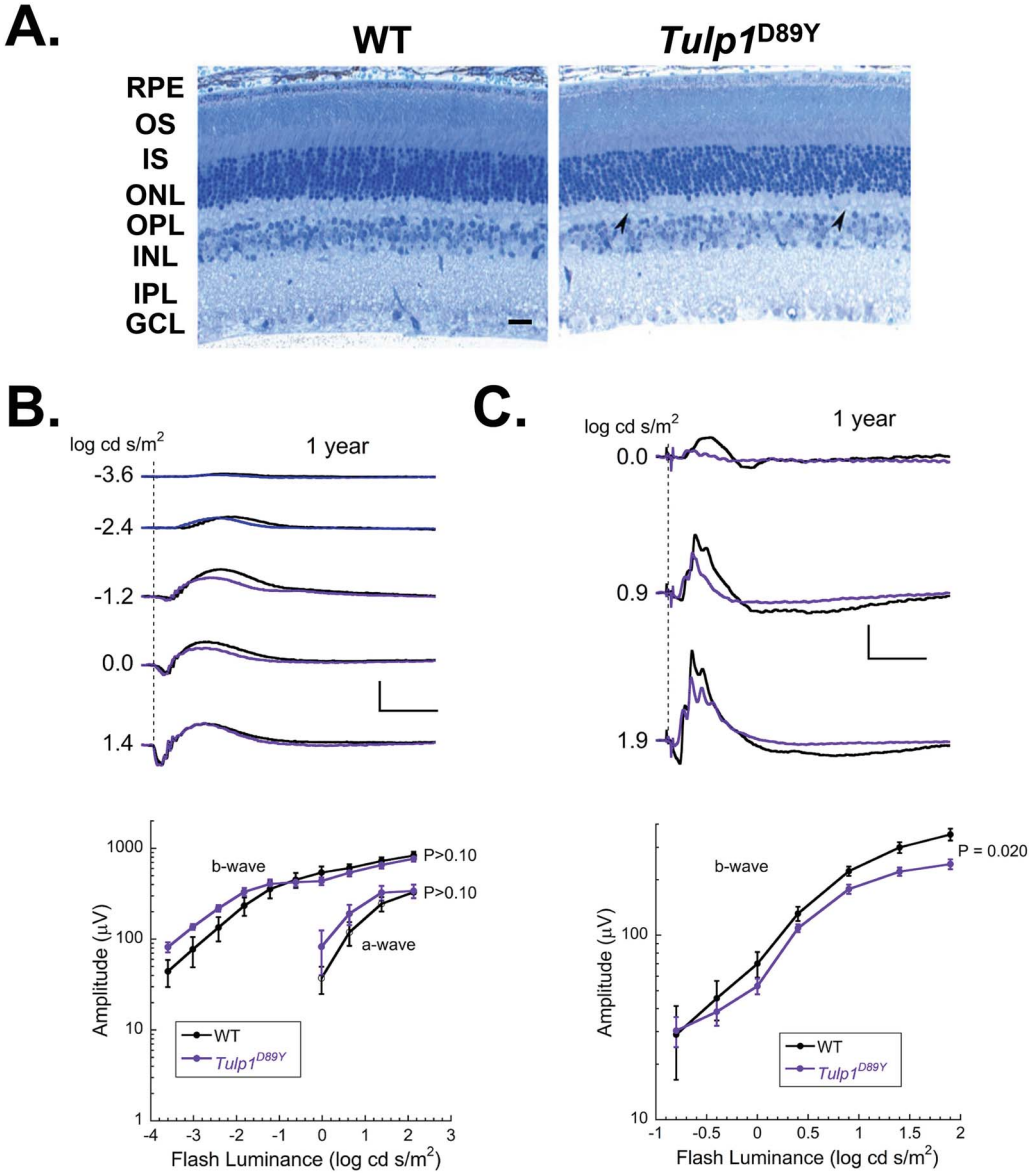

Figure 8. Age-related defects in *Tulp1*^{D89Y} mice. (A) Retinal histological sections stained with toluidine blue at 12 months of age. There are minimal changes in the *Tulp1*^{D89Y} retina compared to WT, aside from slightly less RPE pigmentation and presence of dilated structures in the OPL (black arrowheads). Scale bar = 20 um. Dark-adapted (B) and light-adapted (C) ERG analysis of WT and *Tulp1*^{D89Y} mice tested at 12 months of age. In each panel, the upper plot compares representative waveforms while the lower panels present summary luminance-response functions for the ERG a- or b-waves. Scale bars indicate 500 μV vs 100 ms in (B) and 100 μV vs 100 ms in (C). Data points indicate the average (±SEM) for 4–6 mice. RPE: Retinal pigment epithelium, OS: Outer segment, IS: Inner segment, ONL: Outer nuclear layer, OPL: Outer plexiform layer, INL: Inner nuclear layer, IPL: Inner plexiform layer, GCL: Ganglion cell layer.

models of *Tulp1* exist, which completely lack expression of the protein in the retina [20, 24]. Here, we report the generation of two novel mouse models of IRD, each caused by a different *TULP1* homozygous missense mutation documented in patients. The *Tulp1*^{D89Y} mouse corresponds to the D94Y mutation reported in a patient with LCA [25] while the *Tulp1*^{F492L} mouse corresponds to the F491L mutation reported in patients with ARRP and CRD [4, 10]. Evaluating these new mouse models circumvents the compensation and redundancy of endogenous *Tulp1* of previous *in vitro* and transiently-expressing *in vivo* experiments and provides relevant mouse models of *TULP1*-associated IRDs caused by missense mutations. In both knock-in models the distribution of mutant TULP1 protein in photoreceptors is indistinguishable to WT. Our comprehensive and comparative analyses across *Tulp1* mutant models report two major findings: 1) Strikingly variable retinal phenotypes between the different *Tulp1* genetic models, leading to novel information regarding domain-specific mutations and consistent with the spectrum of human *TULP1*-associated IRDs; and 2) Activation of the most evolutionarily conserved branch of the ER-UPR stress response pathway in two early-onset, rapid, progressive photoreceptor degeneration mutant models, *Tulp1*^{F492L} and *Tulp1*$^{-/-}$.

Tulp1 ^{F492L} mice undergo an early-onset, rapid photoreceptor degeneration, similar to the time course seen in *Tulp1*$^{-/-}$ mice. The *Tulp1*^{F492L} retinal morphology and function correlate and reveal a progressive degeneration involving both rod and cone photoreceptors with a significant decrease in ONL thickness starting to occur at P23 compared to WT. Defects at the distal end of the photoreceptor cell observed in both the *Tulp1*^{F492L} and *Tulp1*$^{-/-}$ mouse models include the mistrafficking of rhodopsin and both cone

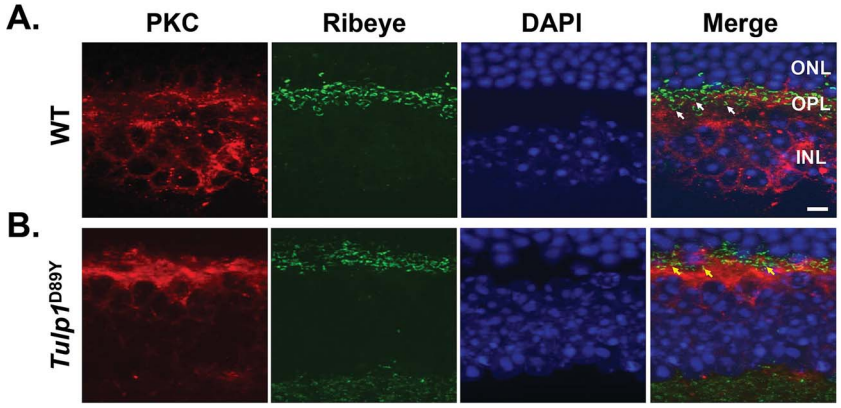

Figure 9. Relationship between presynaptic and postsynaptic photoreceptor elements in 12 months old *Tulp1*^{D89Y} retinas. (A) In the WT OPL, PKC-labelled rod bipolar cells (red) show long and branching dendrites stretching toward the photoreceptor terminals that are stained with Ribeye-immunoreactive (green) horseshoe-shaped ribbons (white arrows). (B) In the *Tulp1*^{D89Y} OPL, bipolar cell dendrites show shortened appendages with reduced branching, and Ribeye-immunoreactive ribbons appear punctate (yellow arrows). Blue indicates nuclear DAPI stain. Scale bar = 5 um. ONL: Outer nuclear layer, OPL: Outer plexiform layer, INL: Inner nuclear layer.

opsins from the IS through the transition zone to the OS, a modified primary cilium enriched with OS-specific phototransduction and structural proteins. It is well-established that the signature tubby domain of TULP proteins interacts and binds specifically with the phosphoinositide, PI(4,5)P_2, of the plasma membrane [38–40]. Several reports studying the ubiquitously-expressed TULP3 protein indicate that it is through this interaction whereby TULP3 traffics a variety of cargos to the ciliary membrane of other organs such as brain, liver and kidney [41–43]. Although residue 492 in the tubby domain of TULP proteins is not directly involved in binding the lipid head-groups or phosphate-groups of PI(4,5)P_2, it is located in the unique helix-filled barrel structure required for phosphoinositol binding and is highly conserved across species, indicating it's importance [16, 38, 39, 44]. Substitution of this phenylalanine likely alters tubby domain interactions or changes the 3-dimentional protein shape, causing structural disruption in this critical region. Indeed, our *in vitro* studies have shown that TULP1^{F492L} mutant protein mislocalizes to the ER and *in silico* computational analysis have reported that this mutation causes structural destabilization and folding defects leading to ER stress [28]. Defects at the proximal end of the photoreceptor cell were also observed in both *Tulp1*$^{-/-}$ and *Tulp1*^{F492L} mice where synaptic ribbons, specialized for continuous neurotransmitter release to downstream second-order neurons, appear malformed and are not organized into the horseshoe-shape characteristic of WT ribbons. The synapses also appear reduced in number, indicating an overall loss in OPL density. Our group and others have shown that TULP1 binds Ribeye, the primary structural protein of the ribbon synapse, which is required to maintain synaptic ribbon integrity [45–47]. Several *TULP1* mutations located in the tubby domain, including F492L, abolish the interaction of TULP1 with Ribeye [23]. Interestingly, both TULP1 and PI(4,5)P_2 co-localize to the periactive zone of the ribbon synapse, a region surrounding the ribbon enriched in endocytic activity where PI(4,5)P_2 is a well-known signaling lipid important for initiating endocytosis [48–50]. These synaptic morphological deficits correlate with the rod and cone early-onset functional defects seen in both *Tulp1*$^{-/-}$ and *Tulp1*^{F492L} mutant mice. Taken together, these findings strongly support the idea that the F492L mutation disrupts a key region in the tubby domain required for photoreceptor vesicular trafficking of proteins from the IS to the OS and the vesicular endocytosis and exocytosis required at the ribbon synapse.

In stark contrast to the *Tulp1*^{F492L} phenotype, our results indicate that the D89Y mutation does not cause severe photoreceptor degeneration but rather, at least in mouse, a late-onset, mild phenotype primarily affecting the photoreceptor synaptic connections to the depolarizing bipolar cells (DBCs) and likely a secondary effect involving the RPE. A reduced cone ERG b-wave amplitude was observed in the *Tulp1*^{D89Y} model similar to the *Tulp1*^{F492L} and *Tulp1*$^{-/-}$ models, however at a much later timepoint. This functional defect is likely due to thinning of the OPL along with the presence of dilated structures. We also observed hypopigmentation changes in the RPE of the *Tulp1*^{D89Y} mouse at 12 months of age. This hypopigmentation of the RPE may be due to a decline in melanin content known to occur with age [51]. It is also possible that the slow photoreceptor degeneration that is occurring exacerbates in the RPE due to chronic stress related to disturbed homeostasis of endocytosis, phagocytosis, ER-UPR, or autophagy, all processes involved in the intracellular digestion and recycling of cellular components [51, 52].

The distinct retinal phenotypes observed in our *Tulp1* mouse models correspond to structural studies performed on the tubby domain of TULP3 which demonstrated that there are specific surface residues involved in trafficking of integral membrane proteins to the cilia of organs such as brain, liver and kidney [41–43]. Our results support this idea and suggest that mutations affecting the tubby domain in TULP1 cause the mistrafficking of proteins to the photoreceptor OS. We found that the D89Y mutation, located in the N-terminal intrinsically disordered region (IDR) of TULP1, did not cause OS protein mistrafficking. However, this mutation is 100% conserved across all mammalian species surveyed, potentially disrupting the protein's folding pattern and may therefore partially abrogate Tulp1 function, resulting in hypomorphic behavior. Indeed, it has been proposed that *TULP1* missense mutations not affecting the tubby domain may result in later onset disease with milder phenotypes [36]. The amino termini of TULP proteins are diverse and have been proposed to direct distinct functions. For example, a short domain in the IDR (A.A. 23–68) enables some TULP members such as TULP3, TULP2 and TUB; but not TULP1 and TULP4, to bind to intraflagellar transport complex-A [41]. This embedded motif confers the ability of TULP3 to traffic specific cargo [53].

Another observation we noted between our mutant models was that the photoreceptor degeneration was slightly milder in the

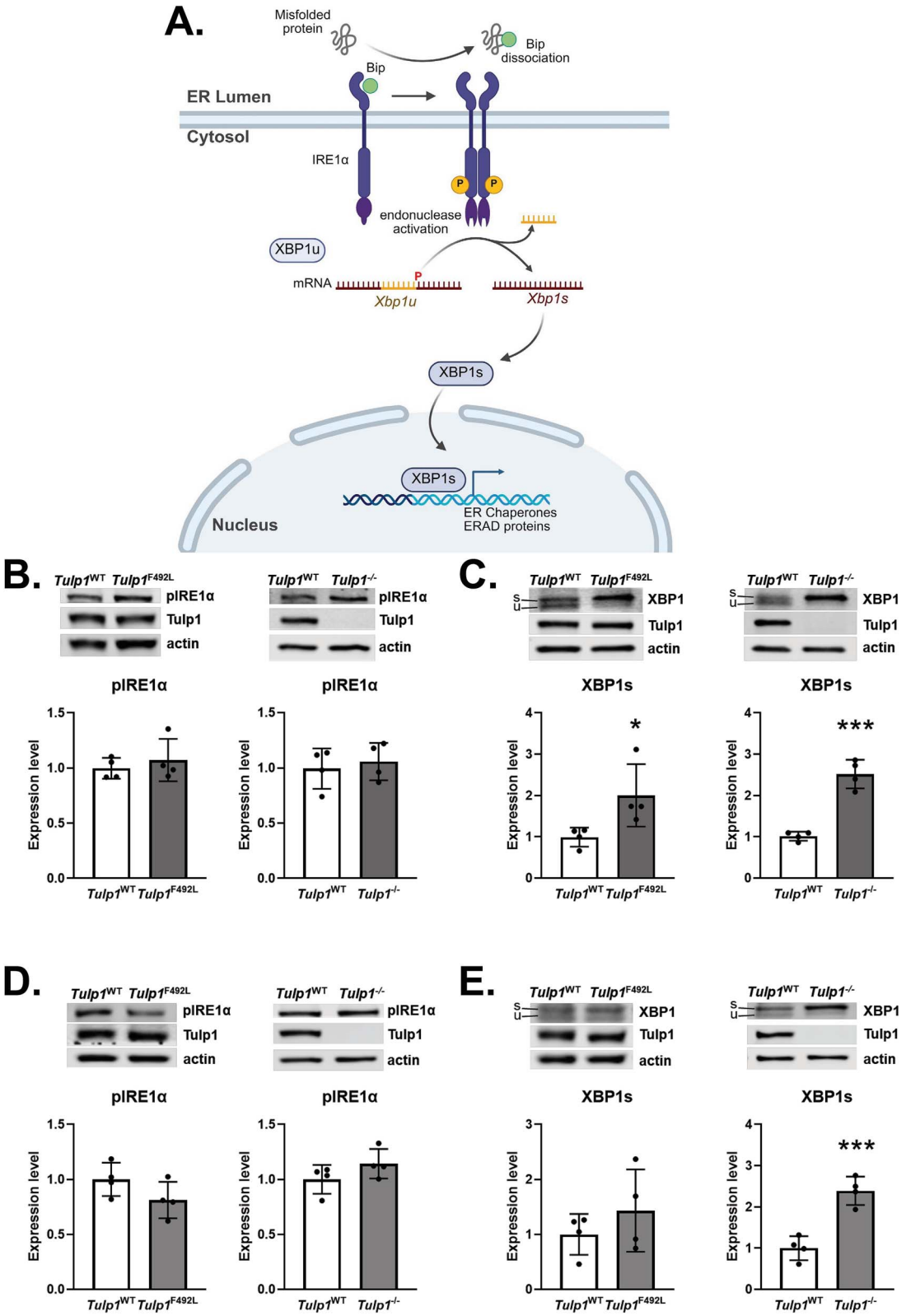

Figure 10. ER-UPR activation in Tulp1 mutant mice. (A) a simplified schematic of the IRE1-XBP1 branch of the ER-UPR pathway. Made with BioRender. (B) Western blot analysis of retinal lysate from P30 *Tulp1*^{F492L} and *Tulp1*$^{-/-}$ mice express comparable levels of activated IRE1 as in WT mice ($P = 0.63$ and $P = 0.52$, respectively). (C) Western blot analysis of retinal lysate from P30 *Tulp1*^{F492L} and *Tulp1*$^{-/-}$ mice express statistically significantly higher levels of XBP1s than WT retina ($P = 0.04$ and $P = 0.0002$, respectively). (D) Western blot analysis of retinal lysate from P17 *Tulp1*^{F492L} and *Tulp1*$^{-/-}$ mice express comparable levels of activated IRE1 compared to WT mice ($P = 0.14$ and $P = 0.18$, respectively). (E) Western blot analysis of retinal lysate from P17 *Tulp1*$^{-/-}$ mice express statistically significantly higher levels of XBP1s than WT retina ($P = 0.0008$). Two-tailed Student's t-test, $^{*}P < 0.05$, $^{***}P < 0.001$. n = 4 mice for each group.

Tulp1^{F492L} retina than in the *Tulp1*$^{-/-}$ retina, as evidenced by the presence of more photoreceptor nuclei in the *Tulp1*^{F492L} retina at both P23 and 1 month of age. This observation shows the benefit of having the presence of a full-length (although mutant) TULP1 protein in photoreceptors and further suggests an independent function of the TULP1 N-terminal domain. Our findings suggest that this region may impart a yet unknown synaptic-specific function vital to photoreceptor cells.

A striking feature attributed to *TULP1*-associated IRDs is clinical heterogeneity. However, our knowledge of phenotypic differences between N- and C-terminus mutations is limited, as patients often present late with varying manifestation of disease. The F491L mutation was originally identified in an ARRP patient that was a compound heterozygote carrying another *TULP1* missense change in the C-terminal tubby domain [4]. The clinical data for this patient indicated that at 31 years of age, he had best-corrected visual acuities of less than 20/200 in both eyes, had less than 30 degrees of central visual field diameter remaining, and his ERG responses could not be detected. The second patient having the F491L mutation was also a compound heterozygote having a second *TULP1* splice site mutation occurring in the tubby domain [10]. At age 37, he was diagnosed with cone-rod dystrophy, had best corrected visual acuities of less than 20/600 in both eyes, had pericentral scotomas, and flat ERG's. Our *Tulp1*^{F492L} mouse phenotype, expressing an ortholog mutation, mirrored that seen in patients, manifesting an early-onset, rapid, progressive photoreceptor degeneration. The D94Y homozygous missense mutation was identified through homozygous mapping in a consanguineous Arab-Muslim family with a single child affected with LCA [25]. The clinical data available for this individual described that his ERG was non-detectable at six years of age. To our knowledge, this is the only *homozygous* missense mutation identified in the N-terminal divergent region. It's interesting that the observed phenotype in our *Tulp1*^{D89Y} model does not mirror the clinical presentation observed in the human patient with the orthologous mutation. There are several possibilities why this might have occurred: 1) This *TULP1* variant is not the cause of LCA in the reported individual. Due to the lack of detailed genome sequencing information, we cannot rule out the possibility that this patient also carries another mutation in the *TULP1* gene, possibly affecting the tubby domain; or the patient may harbor mutations in another gene that contributes to his LCA diagnosis. 2) The phenotypic effects of the mutation are different between human and mouse. 3) There are genetic background, genetic modifiers, or environmental factors modulating the variable phenotype seen between human and mouse.

Advancements in our understanding of the molecular mechanism involved in *TULP1*-associated IRD is vital toward facilitating the development of a therapy to slow or halt disease progression. We have observed defects at the distal and proximal ends of the photoreceptor cell including mistrafficking of OS proteins and synaptic malformation in *Tulp1*^{F492L} and *Tulp1*$^{-/-}$ mutant retinas. In addition, our previous *in vitro* experiments have shown missense mutations in *Tulp1* express as misfolded protein products that accumulate within the ER causing prolonged ER stress and *in-silico* computational analysis has predicted that missense mutations limited to the tubby domain had decreased protein stability [28]. Destabilization, folding defects and mistrafficking of proteins are commonly associated with increased ER stress which can trigger the activation of UPR pathways. Due to the continual process of OS shedding and renewal each day, the highly compartmentalized photoreceptors have a tremendously high protein turnover rate and coordinated protein trafficking mechanisms [54]. Proteins that localize to improper cellular compartments due to mutations can lead to aggregation, incorrect interactions, or dysregulated functions, requiring degradation. Therefore, examining protein quality through the ER and balancing protein homeostasis through the UPR pathway is critical in maintaining photoreceptor function and survival [31, 55]. The Inositol-requiring enzyme type 1 (IRE1) pathway is the most evolutionary conserved UPR branch and numerous studies have confirmed the upregulation of activated IRE1 in the pathogenesis of several neurodegenerative disorders associated with the accumulation of mistrafficked and misfolded proteins followed by the induction of ER stress [29, 30, 32]. When mistrafficked and misfolded proteins are sensed by the N-terminal ER luminal domain of IRE1, the C-terminal cytoplasmic region initiates downstream responses through two functional motifs: one possessing serine/threonine kinase activity and the other containing the endoribonuclease (RNase) activity [32]. The latter becomes activated via conformational change, autophosphorylation, and higher-order assembly. Activated IRE1a induces the unconventional spicing of X-box binding protein 1 mRNA unspliced (XBP1u) to spliced XBP1 (XBP1s). XBP1s encodes a transcription factor that regulates expression of a large group of UPR downstream genes including chaperones, genes involved in ER-associated degradation (ERAD), ER biogenesis and lipid synthesis [56, 57]. Here, for the first time, we report activation of the IRE1-XBP1 branch of ER-UPR pathway associated with either the absence of TULP1 protein or in the presence of a missense mutation in the C-terminal tubby domain of TULP1. Activation of the ER-UPR pathway is likely due to mistrafficking of OS proteins in *Tulp1*^{F492L} and *Tulp1*$^{-/-}$ retinas, observed as early as P17, prior to onset of degenerative cell loss and statistically significant at mid-stage of degeneration at P30. Very recently, it has been shown that ER stress due to mislocalized rhodopsin in the photoreceptor synapse can also cause disruption of other synaptic protein complexes thereby altering trans-synaptic signaling, a defect observed here in our mutant *Tulp1* models [58].

In summary, the phenotypic differences in *Tulp1*^{F492L} and *Tulp1*^{D89Y} retinas showcase the wide spectrum in disease pathophysiology and suggest a domain-dependent prognosis of *TULP1* missense mutations. The *Tulp1*^{F492L} model recapitulates the early-onset progressive photoreceptor degeneration observed in human patients. The spatial and temporal degeneration process is very similar to that observed in *Tulp1*$^{-/-}$ mice and strongly stresses the importance of the C-terminal tubby domain in TULP1 protein function. Although the phenotype observed in the *Tulp1*^{D89Y} model is later-onset, this novel mouse line provides a much-needed tool to study TULP1 N-terminal-specific mutations relevant to synaptic proteins. A prominent pathological feature of both the *Tulp1*^{F492L} and *Tulp1*$^{-/-}$ models is opsin mislocalization, a characteristic also seen in patients with IRDs and retinal ciliopathies. By identifying the ER-UPR as a key causative mechanism of photoreceptor cell death in *Tulp1*^{F492L} and *Tulp1*$^{-/-}$ mice, we can begin to link pathway intermediates that can be targeted by known pharmacological modulators to delay or slow photoreceptor degeneration in our *Tulp1* mutant models. Furthermore, our findings facilitate direct genotype–phenotype correlation and combined with photoreceptor cell exclusivity, promote TULP1 as a model for combining disease mechanisms and therapy for several forms of IRDs.

Materials and methods

Animals

All experiments on animals were approved by the Institutional Animal Care and Use Committee of the Cleveland Clinic and were performed in compliance with the ARVO Statement for the Use

of Animals in Ophthalmic and Vision Research. The generation of *Tulp1*$^{-/-}$ mice has been described previously and is maintained on a C57BL/6 J background [20]. WT C57BL/6 J mice were purchased from Jackson Laboratory (Bar Harbor, Maine). All lines were confirmed negative for the *rd1* and *rd8* mutations [59, 60]. For all tissue collections, mice were euthanized by carbon dioxide inhalation followed by cervical dislocation.

Generation of *Tulp1*^{D89Y} and *Tulp1*^{F492L} knock-in mice

Tulp1 mutant knock-in mouse models were generated by CRISPR/Cas9 gene editing technology. To mutate D89 in exon 4 and F492 in exon 14 of the mouse *Tulp1* gene, the genomic sequence surrounding each codon's respective exon was analyzed using crispr.genome-engineering.org. The cutting efficiencies of candidate guides were evaluated and screened using the Guide-it sgRNA screening system (Takara Bio). For D89Y, sgRNA #11 (CAAGTTCCTGAGGGACCCCG) was selected and ordered as an injection-ready in-vitro transcription sgRNA from PNAbio, along with Cas9 nuclease protein. A single-stranded 100 bp microhomology DNA template, Tulp1-D89Y-100mer, (GACTCGGCAGAGCCGCGCGCTGCGCAGACAGTCTACGCCAAGT TCCTGAGGTACCCCGAAGCCAAGAAGCGGGACCCCCGGGAAAAC TTCCTAGTTGCCC), which mutates D89 to Y and contains a silent mutation to eliminate further cutting by Cas9 (both mutations introduced are underlined), was synthesized as a PAGE purified Ultramer (Integrated DNA Technologies). For F492L, sgRNA #3 (AATCTGAAAGTTCTTGACGG) was selected and ordered as injection ready in vitro transcription sgRNA from PNAbio, along with Cas9 nuclease protein. A single-stranded 100 bp microhomology DNA template, Tulp1-F492L-100mer (CCTACACCCTCAACTTCCAGGGCCGCGTCACCCAGGCTTCCGTCA AGAACCTCCAGATTGTGCACGCTGATGACCGTGAGTATCTGAGGG CCACCCAGAC), which mutates F492 to L and contains a silent mutation to eliminate further cutting by Cas9 (all three mutations introduced are underlined), was synthesized as a PAGE purified Ultramer (Integrated DNA Technologies). Following standard transgenic practice, a range of mixtures, starting from 5 ng/μl Cas9 protein, 5 ng/μl sgRNA, and 5 ng/μl oligo to 50 ng/μl Cas9 protein, 50 ng/μl sgRNA, and 50 ng/μl oligo were microinjected by the Case Transgenic and Targeting Facility of Case Western Reserve University School of Medicine (Cleveland, OH) into the pronucleus of one cell stage C57BL/6 J embryos. Injected embryos were surgically transferred to pseudo pregnant recipient females (CD1), and the resulting pups were crossed to generate the homozygous lines studied here.

Genotyping of *Tulp1*^{D89Y} and *Tulp1*^{F492L} knock-in mice: DNA from founder animals was subjected to direct sequencing to confirm precise integration of the targeted mutation and to verify the absence of sequence alterations surrounding the integration site. Genomic DNA extracted from the tails of mice was PCR amplified and sequenced using the following primers: exon 4 (D89Y) forward primer 5′- GGAAGCACGAGGAGCCGCCCGCA—3′; exon 4 reverse primer 5′- GGTCTGGGGCGCGGGCAACTAGGA—3′; exon 14 (F492L) forward primer 5′—GGCTGCTAGTGCGCTGGCAGAACA—3′; exon 14 reverse primer 5′—TCTGGGTGGCCCTCAGATACTCAC—3′. Germline transmission was achieved, and genotypes of offspring were also verified by direct sequence analysis. To reduce any potential off-target effects generated by the CRISPR/Cas9 system, guide RNAs were selected with the help of several bioinformatic algorithms. Both mutant lines underwent a minimum of five backcrosses with WT mice and the Tulp1 locus was deep sequenced.

Immunohistochemistry

Following euthanasia, eyes were enucleated and immediately frozen in OCT with liquid nitrogen and stored at -80°C. Tissue was sectioned at 10-μm thickness with a cryostat (Leica, Wetzlar, Germany) at −20°C. Retinal sections were fixed in 4% paraformaldehyde (PFA) for 5 mins, followed by brief washing in 1X PBS. Sections were permeabilized with 1X PBS containing 0.025% Triton X-100 (PBST) for 10 mins and then washed 3 times with 1X PBS, 5 mins each. Slides were then incubated with blocking solution (1% BSA and 10% Donkey serum in freshly prepared 1X PBS) for 2 hrs at room temperature (RT) and then subsequently incubated with target primary antibodies (diluted in 1X PBS with 1% BSA) overnight at 4°C. Primary antibodies and dilutions were as follows: rabbit polyclonal M-Tulp1N at 1:250 [19]; mouse monoclonal Ribeye/CtBP2 at 1:500 (# 612044; BD Biosciences, San Jose, CA); rabbit polyclonal Protein Kinase C-α (PKC) at 1:1000 (# sc-208; Santa Cruz Biotechnology Inc., Santa Cruz, CA); mouse monoclonal Rhodopsin at 1:2000 (# ab98887, Abcam, Cambridge, UK); rabbit polyclonal M-opsin at 1:500 (# AB5405, Millipore Corp, Burlington, MA); rabbit polyclonal S-opsin at 1:500 (AB5407, Millipore Corp, Burlington, MA) and rabbit polyclonal Peripherin at 1:500 (pAbMPCT, gift from Dr Andrew F.X. Goldberg, Oakland Univ., Rochester, MI [21, 61]) dilutions. After removal of primary antibody, the slides were washed 3 times with 1X PBST on a rocker for 5 mins each. Slides were then incubated with secondary antibodies (AlexaFluor 488 goat anti–rabbit IgG, AlexaFluor 488 goat anti–mouse IgG, AlexaFluor 594 goat anti–rabbit IgG and AlexaFluor 594 goat anti–mouse IgG (Invitrogen, Carlsbad, CA)) at 1:1000 dilution in 1X PBS with 1% BSA in the dark for 1 hr at RT. Slides were then washed 3 times with 1X PBST 10 mins each and mounted with mounting media containing DAPI (Vectashield). Co-staining of Tulp1 and Acetyl-α Tubulin were performed by staining the slides with M-Tulp1N at 1:400 dilution first, followed by staining with mouse monoclonal Acetyl-α Tubulin at 1:400 dilution (# 32–2700, Invitrogen, Carlsbad, CA) using the Mouse on Mouse Immunodetection kit (BMK-2202, Vectorlabs, Newark, CA). All slides were stored in the dark before being imaged using a fluorescence microscope (Zeiss Axio Imager. Z2).

Histology

Enucleated eyes were fixed overnight at 4°C in 2% paraformaldehyde, 2.5% glutaraldehyde, and 0.001% $CaCl_2$ in 0.1 M cacodylate buffer. After removal of the anterior segments using a dissecting microscope, eyecups were processed for epon embedding as previously described [62]. Semi-thin 750 nm sections were cut using a diamond knife (DiATOME, Hatfield, PA), collected on glass slides, and stained with toluidine blue. Images of eyecup sections (extending to the ora serrata) were acquired under identical settings with a Zeiss Axioimager Z1 and MRc5 camera (Carl Zeiss AG, Oberkochen, Germany). Images were exported to ImageJ v1.54g software (NIH, Bethesda, MD) and calibrated using an embedded reference scale. The thickness of the outer nuclear layer (ONL) was measured using the ImageJ v1.54g software by taking three measurements at ∼200 μm from the optic nerve head at each side (dorsal and ventral region). The average of six measurements was reported as the ONL thickness value for each mouse. At least n = 3 animals were included in ONL thickness quantification for each group.

Electroretinography

After overnight dark adaptation, mice were anesthetized with ketamine (80 mg/kg) and xylazine (16 mg/kg). Eyedrops were used to anesthetize the cornea (1% proparacaine HCl) and to dilate the pupil (1% mydriacyl, 2.5% phenylephrine HCl, 1% cyclopentolate HCl). Mice were placed on a temperature-regulated heating pad throughout the recording session. ERGs were recorded with a stainless-steel electrode that made contact with the corneal surface through a thin layer of methylcellulose. Needle electrodes placed in the cheek and the tail served as reference and ground leads, respectively. Responses were obtained under dark-adapted and then light-adapted conditions. For the dark-adapted series, a total of ten strobe stimuli ranging from −3.6 to 2.1 log candela (cd) s/m^2 were presented in order of increasing flash strength. As flash strength increased, the number of successive trials that were averaged decreased from 20 to 2 and the interstimulus interval increased from 4 to 90 s. A steady 30 cd/m^2 achromatic adapting field then was presented in the ganzfeld bowl. After 7 min of light adaptation, cone ERGs were obtained to a series of seven strobe flash stimuli ranging from −1 to 2 log cd s/m^2 that were superimposed upon this field. At each stimulus level, a series of 50 successive responses were averaged to stimuli delivered at 2.1 Hz.

The amplitude of the a-wave was measured from the pre-stimulus baseline to the value observed at 8 ms after the flash presentation. The dark-adapted b-wave amplitude was measured from the a-wave amplitude trough to the peak of the b-wave. The amplitude of the light-adapted ERG b-wave was measured from the initial negative trough to the peak of the response. ERG data are presented as a mean ± s.e.m. Statistical significance was assessed using a two-way repeated measures analysis of variance (ANOVA).

Western blot analysis

Total protein was isolated from two retinas of a single mouse using RIPA protein lysis buffer (#J63306 Thermo Scientific) containing protease inhibitors and phosphate inhibitors. Approximately 20 μg of total protein was electrophoresed on 4–12% SDS-PAGE gels and then transferred to PVDF membranes. Membranes were probed with primary antibodies against pIRE1a (1:500 dilution, Novus, NB100–2323), XBP1 (1:500 dilution, Santa Cruz, sc-7160), TULP1 (1:2000 dilution [19]) and β-actin (1:4000 dilution, Cell signaling #3700) in LI-COR Intercept (TBS) Blocking Buffer (#927–60 001). Corresponding secondary antibodies were applied at 1:10000 dilution. The membranes were imaged, and the intensity of targeting bands were quantified using Licor Odyssey CLx system. Relative intensities of each band were quantified (densitometry) using the Image Studio software version 5.2 and normalized to the loading control, β-actin.

Statistical analyses

Results are presented as mean ± s.d. or mean ± s.e.m. and the number of biological replicates for each experiment is indicated in the figure legends. All determinations for each experiment were performed at least in duplicate. Statistical significance was assessed using the two-tailed Student's t-test or two-way ANOVA.

Acknowledgements

We thank Craig Beight for maintaining the animal colony, Maximillion Campbell for helping with histological sections and Kaneshia B Freeman for helping with the manuscript revision. We thank the Case Transgenic and Targeting Facility and the Genomics Core at Case Western Reserve University School of Medicine (Cleveland, OH) for generating and identifying the *Tulp1* knock-in mice.

Author contributions

Ke Jiang (Data curation, Formal analysis, Writing—original draft, Writing—review & editing), Satyabrata Sinha (Data curation, Formal analysis), Vera L Bonilha (Data curation, Formal analysis), Minzhong Yu (Data curation, Formal analysis), Neal S Peachey (Data curation, Formal analysis, Writing—original draft, Writing—review & editing), Stephanie A Hagstrom (Conceptualization, Data curation, Formal analysis, Funding acquisition, Writing—original draft, Writing—review & editing).

Conflict of Interest statement: The authors have no financial, personal, professional, or other conflict of interests to declare.

Funding

This work was supported by the National Institutes of Health [EY032459 to S.A.H, EY027750 to V.L.B.]; and P30 EY025585; and an Unrestricted Award from Research to Prevent Blindness; and VA Office of Research & Development [IK6 BX005233 to N.S.P.]; and Cleveland Clinic startup funds to V.L.B.; and funds from the Timken Foundation to V.L.B.; and funds from the Dale and Lois Marks & Family to V.L.B.

References

1. Hanany M, Shalom S, Ben-Yosef T. *et al.* Comparison of worldwide disease prevalence and genetic prevalence of inherited retinal diseases and variant interpretation considerations. *Cold Spring Harb Perspect Med* 2024;**14**. https://doi.org/10.1101/cshperspect.a041277.
2. Schofield D, Kraindler J, Tan O. *et al.* Patient-reported health-related quality of life in individuals with inherited retinal diseases. *Ophthalmol Sci* 2022;**2**:100106. https://doi.org/10.1016/j.xops.2021.100106.
3. Duncan JL, Bowman A, Laster A. *et al.* Inherited retinal degenerations and non-Neovascular age-related macular degeneration: progress and unmet needs. *Transl Vis Sci Technol* 2024;**13**:28. https://doi.org/10.1167/tvst.13.12.28.
4. Hagstrom SA, North MA, Nishina PL. *et al.* Recessive mutations in the gene encoding the tubby-like protein TULP1 in patients with retinitis pigmentosa. *Nat Genet* 1998;**18**:174–176. https://doi.org/10.1038/ng0298-174.
5. Lewis CA, Batlle IR, Batlle KG. *et al.* Tubby-like protein 1 homozygous splice-site mutation causes early-onset severe retinal degeneration. *Invest Ophthalmol Vis Sci* 1999;**40**:2106–2114.
6. Mataftsi A, Schorderet DF, Chachoua L. *et al.* Novel TULP1 mutation causing leber congenital amaurosis or early onset retinal degeneration. *Invest Ophthalmol Vis Sci* 2007;**48**:5160–5167. https://doi.org/10.1167/iovs.06-1013.
7. den Hollander AI, van Lith-Verhoeven JJ, Arends ML. *et al.* Novel compound heterozygous TULP1 mutations in a family with severe early-onset retinitis pigmentosa. *Arch Ophthalmol* 2007;**125**:932–935. https://doi.org/10.1001/archopht.125.7.932.
8. Roosing S, van den Born LI, Hoyng CB. *et al.* Maternal uniparental isodisomy of chromosome 6 reveals a TULP1 mutation as a novel

cause of cone dysfunction. *Ophthalmology* 2013;**120**:1239–1246. https://doi.org/10.1016/j.ophtha.2012.12.005.
9. Guo Y, Prokudin I, Yu C. *et al.* Advantage of whole exome sequencing over allele-specific and targeted segment sequencing in detection of novel TULP1 mutation in Leber congenital Amaurosis. *Ophthalmic Genet* 2015;**36**:333–338. https://doi.org/10.3109/13816810.2014.886269.
10. Bodenbender JP, Marino V, Bethge L. *et al.* Biallelic variants in TULP1 are associated with heterogeneous phenotypes of retinal dystrophy. *Int J Mol Sci* 2023;**24**:2709. https://doi.org/10.3390/ijms24032709.
11. Ullah I, Kabir F, Iqbal M. *et al.* Pathogenic mutations in TULP1 responsible for retinitis pigmentosa identified in consanguineous familial cases. *Mol Vis* 2016;**22**:797–815.
12. Dockery A, Stephenson K, Keegan D. *et al.* Target 5000: target capture sequencing for inherited retinal degenerations. *Genes (Basel)* 2017;**8**:304.
13. Stone EM, Andorf JL, Whitmore SS. *et al.* Clinically focused molecular investigation of 1000 consecutive families with inherited retinal disease. *Ophthalmology* 2017;**124**:1314–1331. https://doi.org/10.1016/j.ophtha.2017.04.008.
14. Hanany M, Rivolta C, Sharon D. Worldwide carrier frequency and genetic prevalence of autosomal recessive inherited retinal diseases. *Proc Natl Acad Sci USA* 2020;**117**:2710–2716. https://doi.org/10.1073/pnas.1913179117.
15. Jaffal L, Joumaa H, Mrad Z. *et al.* The genetics of rod-cone dystrophy in Arab countries: a systematic review. *Eur J Hum Genet* 2021;**29**:897–910. https://doi.org/10.1038/s41431-020-00754-0.
16. Mukhopadhyay S, Jackson PK. The tubby family proteins. *Genome Biol* 2011;**12**:225. https://doi.org/10.1186/gb-2011-12-6-225.
17. North MA, Naggert JK, Yan Y. *et al.* Molecular characterization of TUB, TULP1, and TULP2, members of the novel tubby gene family and their possible relation to ocular diseases. *Proc Natl Acad Sci USA* 1997;**94**:3128–3133. https://doi.org/10.1073/pnas.94.7.3128.
18. Wang M, Xu Z, Kong Y. The tubby-like proteins kingdom in animals and plants. *Gene* 2018;**642**:16–25. https://doi.org/10.1016/j.gene.2017.10.077.
19. Hagstrom SA, Adamian M, Scimeca M. *et al.* A role for the tubby-like protein 1 in rhodopsin transport. *Invest Ophthalmol Vis Sci* 2001;**42**:1955–1962.
20. Hagstrom SA, Duyao M, North MA. *et al.* Retinal degeneration in tulp1−/− mice: vesicular accumulation in the interphotoreceptor matrix. *Invest Ophthalmol Vis Sci* 1999;**40**:2795–2802.
21. Grossman GH, Watson RF, Pauer GJ. *et al.* Immunocytochemical evidence of Tulp1-dependent outer segment protein transport pathways in photoreceptor cells. *Exp Eye Res* 2011;**93**:658–668. https://doi.org/10.1016/j.exer.2011.08.005.
22. Grossman GH, Pauer GJ, Narendra U. *et al.* Early synaptic defects in tulp1−/− mice. *Invest Ophthalmol Vis Sci* 2009;**50**:3074–3083. https://doi.org/10.1167/iovs.08-3190.
23. Wahl S, Magupalli VG, Dembla M. *et al.* The disease protein Tulp1 is essential for Periactive zone endocytosis in photoreceptor ribbon synapses. *J Neurosci* 2016;**36**:2473–2493. https://doi.org/10.1523/JNEUROSCI.2275-15.2016.
24. Won J, Shi LY, Hicks W. *et al.* Mouse model resources for vision research. *J Ophthalmol* 2011;**2011**:391384. https://doi.org/10.1155/2011/391384.
25. Beryozkin A, Zelinger L, Bandah-Rozenfeld D. *et al.* Identification of mutations causing inherited retinal degenerations in the israeli and palestinian populations using homozygosity mapping. *Invest Ophthalmol Vis Sci* 2014;**55**:1149–1160. https://doi.org/10.1167/iovs.13-13625.
26. Lee ES, Burnside B, Flannery JG. Characterization of peripherin/rds and rom-1 transport in rod photoreceptors of transgenic and knockout animals. *Invest Ophthalmol Vis Sci* 2006;**47**:2150–2160. https://doi.org/10.1167/iovs.05-0919.
27. Tian G, Ropelewski P, Nemet I. *et al.* An unconventional secretory pathway mediates the cilia targeting of peripherin/rds. *J Neurosci* 2014;**34**:992–1006. https://doi.org/10.1523/JNEUROSCI.3437-13.2014.
28. Lobo GP, Au A, Kiser PD. *et al.* Involvement of endoplasmic reticulum stress in TULP1 induced retinal degeneration. *PLoS One* 2016;**11**:e0151806. https://doi.org/10.1371/journal.pone.0151806.
29. Wodrich APK, Scott AW, Shukla AK. *et al.* The unfolded protein responses in health, aging, and neurodegeneration: recent advances and future considerations. *Front Mol Neurosci* 2022;**15**:831116. https://doi.org/10.3389/fnmol.2022.831116.
30. Gebert M, Slawski J, Kalinowski L. *et al.* The unfolded protein response: a double-edged sword for brain health. *Antioxidants (Basel)* 2023;**12**:1648. https://doi.org/10.3390/antiox12081648.
31. Zhang H, Mu Y, Li H. *et al.* Unfolded protein response in endoplasmic reticulum stress associated with retinal degenerative diseases: a promising therapeutic target. *Neural Regen Res* 2026;**21**:1339–1352. https://doi.org/10.4103/NRR.NRR-D-24-01124.
32. Siwecka N, Rozpedek-Kaminska W, Wawrzynkiewicz A. *et al.* The structure, activation and Signaling of IRE1 and its role in determining cell fate. *Biomedicines* 2021;**9**:156. https://doi.org/10.3390/biomedicines9020156.
33. Peng J, Qin C, Ramatchandirin B. *et al.* Activation of the canonical ER stress IRE1-XBP1 pathway by insulin regulates glucose and lipid metabolism. *J Biol Chem* 2022;**298**:102283. https://doi.org/10.1016/j.jbc.2022.102283.
34. McLaughlin T, Falkowski M, Park JW. *et al.* Loss of XBP1 accelerates age-related decline in retinal function and neurodegeneration. *Mol Neurodegener* 2018;**13**:16. https://doi.org/10.1186/s13024-018-0250-z.
35. Katagiri S, Akahori M, Sergeev Y. *et al.* Whole exome analysis identifies frequent CNGA1 mutations in Japanese population with autosomal recessive retinitis pigmentosa. *PLoS One* 2014;**9**:e108721. https://doi.org/10.1371/journal.pone.0108721.
36. Esteve-Garcia A, Cobos E, Sau C. *et al.* Deciphering complexity: TULP1 variants linked to an atypical retinal dystrophy phenotype. *Front Genet* 2024;**15**:1352063. https://doi.org/10.3389/fgene.2024.1352063.
37. Gonzalez-del Pozo M, Borrego S, Barragan I. *et al.* Mutation screening of multiple genes in Spanish patients with autosomal recessive retinitis pigmentosa by targeted resequencing. *PLoS One* 2011;**6**:e27894. https://doi.org/10.1371/journal.pone.0027894.
38. Boggon TJ, Shan WS, Santagata S. *et al.* Implication of tubby proteins as transcription factors by structure-based functional analysis. *Science* 1999;**286**:2119–2125. https://doi.org/10.1126/science.286.5447.2119.
39. Santagata S, Boggon TJ, Baird CL. *et al.* G-protein signaling through tubby proteins. *Science* 2001;**292**:2041–2050. https://doi.org/10.1126/science.1061233.
40. Xi Q, Pauer GJ, Marmorstein AD. *et al.* Tubby-like protein 1 (TULP1) interacts with F-actin in photoreceptor cells. *Invest Ophthalmol Vis Sci* 2005;**46**:4754–4761. https://doi.org/10.1167/iovs.05-0693.
41. Mukhopadhyay S, Wen X, Chih B. *et al.* TULP3 bridges the IFT-A complex and membrane phosphoinositides to promote trafficking of G protein-coupled receptors into primary cilia. *Genes Dev* 2010;**24**:2180–2193. https://doi.org/10.1101/gad.1966210.

42. Badgandi HB, Hwang SH, Shimada IS. *et al.* Tubby family proteins are adapters for ciliary trafficking of integral membrane proteins. *J Cell Biol* 2017;**216**:743–760. https://doi.org/10.1083/jcb.201607095.
43. Palicharla VR, Badgandi HB, Hwang SH. *et al.* A defined tubby domain beta-barrel surface region of TULP3 mediates ciliary trafficking of diverse cargoes. *Mol Biol Cell* 2025;**36**:ar1. https://doi.org/10.1091/mbc.E24-09-0426.
44. Thallmair V, Schultz L, Zhao W. *et al.* Two cooperative binding sites sensitize PI(4,5)P(2) recognition by the tubby domain. *Sci Adv* 2022;**8**:eabp9471. https://doi.org/10.1126/sciadv.abp9471.
45. Magupalli VG, Schwarz K, Alpadi K. *et al.* Multiple RIBEYE-RIBEYE interactions create a dynamic scaffold for the formation of synaptic ribbons. *J Neurosci* 2008;**28**:7954–7967. https://doi.org/10.1523/JNEUROSCI.1964-08.2008.
46. Schmitz F. The making of synaptic ribbons: how they are built and what they do. *Neuroscientist* 2009;**15**:611–624. https://doi.org/10.1177/1073858409340253.
47. Ebke LA, Sinha S, Pauer GJT. *et al.* Photoreceptor compartment-specific TULP1 Interactomes. *Int J Mol Sci* 2021;**22**:8066. https://doi.org/10.3390/ijms22158066.
48. Di Paolo G, Moskowitz HS, Gipson K. *et al.* Impaired PtdIns(4,5)P2 synthesis in nerve terminals produces defects in synaptic vesicle trafficking. *Nature* 2004;**431**:415–422. https://doi.org/10.1038/nature02896.
49. Wenk MR, De Camilli P. Protein-lipid interactions and phosphoinositide metabolism in membrane traffic: insights from vesicle recycling in nerve terminals. *Proc Natl Acad Sci USA* 2004;**101**:8262–8269. https://doi.org/10.1073/pnas.0401874101.
50. Posor Y, Eichhorn-Grunig M, Haucke V. Phosphoinositides in endocytosis. *Biochim Biophys Acta* 2015;**1851**:794–804. https://doi.org/10.1016/j.bbalip.2014.09.014.
51. Dontsov A, Ostrovsky M. Retinal pigment epithelium pigment granules: norms, age relations and pathology. *Int J Mol Sci* 2024;**25**:3609. https://doi.org/10.3390/ijms25073609.
52. Si Z, Zheng Y, Zhao J. The role of retinal pigment epithelial cells in age-related macular degeneration: phagocytosis and autophagy. *Biomolecules* 2023;**13**:901. https://doi.org/10.3390/biom13060901.
53. Lechtreck K. Cargo adapters expand the transport range of intraflagellar transport. *J Cell Sci* 2022;**135**:260408. https://doi.org/10.1242/jcs.260408.
54. Pearring JN, Salinas RY, Baker SA. *et al.* Protein sorting, targeting and trafficking in photoreceptor cells. *Prog Retin Eye Res* 2013;**36**:24–51. https://doi.org/10.1016/j.preteyeres.2013.03.002.
55. Zhang SX, Wang JJ, Starr CR. *et al.* The endoplasmic reticulum: homeostasis and crosstalk in retinal health and disease. *Prog Retin Eye Res* 2024;**98**:101231. https://doi.org/10.1016/j.preteyeres.2023.101231.
56. Lee AH, Iwakoshi NN, Glimcher LH. XBP-1 regulates a subset of endoplasmic reticulum resident chaperone genes in the unfolded protein response. *Mol Cell Biol* 2003;**23**:7448–7459. https://doi.org/10.1128/MCB.23.21.7448-7459.2003.
57. Sriburi R, Jackowski S, Mori K. *et al.* XBP1: a link between the unfolded protein response, lipid biosynthesis, and biogenesis of the endoplasmic reticulum. *J Cell Biol* 2004;**167**:35–41. https://doi.org/10.1083/jcb.200406136.
58. Thompson SL, Crowder SM, Hekmatara M. *et al.* P23H rhodopsin accumulation causes transient disruptions to synaptic protein levels in rod photoreceptors in a model of retinitis pigmentosa. *Dis Model Mech* 2025;**18**:052256. https://doi.org/10.1242/dmm.052256.
59. Chang B, Hawes NL, Hurd RE. *et al.* Retinal degeneration mutants in the mouse. *Vis Res* 2002;**42**:517–525. https://doi.org/10.1016/S0042-6989(01)00146-8.
60. Mattapallil MJ, Wawrousek EF, Chan CC. *et al.* The Rd8 mutation of the Crb1 gene is present in vendor lines of C57BL/6N mice and embryonic stem cells, and confounds ocular induced mutant phenotypes. *Invest Ophthalmol Vis Sci* 2012;**53**:2921–2927. https://doi.org/10.1167/iovs.12-9662.
61. Goldberg AF, Ritter LM, Khattree N. *et al.* An intramembrane glutamic acid governs peripherin/rds function for photoreceptor disk morphogenesis. *Invest Ophthalmol Vis Sci* 2007;**48**:2975–2986. https://doi.org/10.1167/iovs.07-0049.
62. Bonilha VL, Rayborn ME, Bell BA. *et al.* Retinal histopathology in eyes from patients with autosomal dominant retinitis pigmentosa caused by rhodopsin mutations. *Graefes Arch Clin Exp Ophthalmol* 2015;**253**:2161–2169. https://doi.org/10.1007/s00417-015-3099-7.

Human Molecular Genetics, 2026, 1–17
https://doi.org/10.1093/hmg/ddaf199
Original Article